

Stability and Vibrations of Proteins in Vacuum and Water: Bridging Quantum Accuracy and Force-Field Efficiency

Sergio Suárez-Dou¹, Miguel Gallegos¹, Kyunghoon Han¹,
Florian N. Brünig¹, Joshua T. Berryman¹,
Alexandre Tkatchenko^{1*}

¹Department of Physics and Materials Science, University of Luxembourg, L-1511 Luxembourg City, Luxembourg.

*Corresponding author(s). E-mail(s): alexandre.tkatchenko@uni.lu;
Contributing authors: sergio.suarezdou@uni.lu;
miguel.gallegosgonzalez@uni.lu; kyunghoon.han@uni.lu;
florian.bruenig@uni.lu; josh.berryman@uni.lu;

Abstract

Predicting biomolecular thermodynamics and spectroscopy requires accurate relative energies of metastable states and local curvatures on the potential-energy surface. We show that the general-purpose SO3LR machine-learned force field (MLFF) reproduces PBE0+MBD density-functional theory with unprecedented fidelity across bio-relevant molecules spanning sizes and complexities far beyond its training dataset. For 23 small molecules, SO3LR captures harmonic and anharmonic vibrational features, including frequencies, displacement patterns, and IR spectra. We perform detailed dynamical studies of the amino acid *o*F-Phe⁺, folding of the alanine-15 peptide, and assembly of monomeric p53 transactivation domains into tetramers, in vacuum and water. SO3LR consistently reproduces DFT-level potential-energy surfaces, vibrational densities of states, and mode eigenvectors, capturing anharmonicity, polarization, and medium-range environment-driven interactions crucial for proteins. Our results establish that MLFF-driven dynamics provide a quantum-accurate picture of metastable minima and vibrational properties, achieving DFT-level accuracy at force-field computational cost and opening new possibilities for the computational study of biomolecules.

Introduction

Our understanding of biomolecular structural dynamics has been mainly obtained through static crystal structures, empirical force fields [1, 2], and, more recently, sequence-to-structure tools such as AlphaFold [3]. These approaches have provided invaluable insights into the architecture and local flexibility of proteins, often portraying them as relatively rigid entities with dynamics confined to localized fluctuations around a stable fold [4]. Molecular dynamics (MD) simulations driven by empirical potentials have extended this view by permitting disordered or highly complex motion to be investigated, yet the prevailing paradigm still emphasizes localized motions and modular behavior, often by necessity in order to focus investigation on a region of interest, for example a drug binding pocket. A growing body of experimental evidence suggests that dynamic characteristics away from the better-characterised situations to which classical force fields are targeted may be more complex [5–11].

Beyond localized fluctuations, biomolecular systems explore a hierarchy of metastable states separated by free-energy barriers, which govern slow conformational transitions and functional dynamics. Within each metastable basin, the potential-energy surface (PES) is often well approximated by the harmonic approximation, enabling normal mode analysis (NMA) to extract local curvatures (frequencies) and eigenvectors that encode the principal collective motions. Although this approximation neglects anharmonic couplings and large-amplitude motions, it links local curvature to thermodynamic quantities such as entropic contributions from the vibrational density of states and to spectroscopic observables, since infrared (IR) and Raman intensities depend on mode-resolved dipole and polarizability derivatives [12]. The validity of the harmonic approximation must be assessed to determine whether macroscopic observables, such as transition rates and temperature-dependent conformational changes, can be described accurately.

One critical limitation of conventional MD approaches based on classical force fields is their neglect of quantum-mechanical effects. Quantum phenomena such as polarization, charge transfer, and anharmonic couplings are not only essential for accurate energy landscapes but also manifest directly in vibrational spectra, where subtle shifts and intensity variations encode information about electronic structure and environmental response. Consequently, molecular mechanics force fields (MMFFs) can only be rigorously compared to experiment in regimes where such quantum contributions are negligible, a condition rarely satisfied in biologically relevant systems.

To understand biomolecular stability and vibrations from first principles, we compare widely used MMFFs with modern machine-learned force fields (MLFFs) trained exclusively on quantum-mechanical forces and energies. While MMFFs typically treat two-body electrostatics at all spatial distances using Ewald-like summations, they usually cover non-Coulomb two-body interactions only up to a distance of 8–10 Å and many-body interactions only for the nearest two or three chemical bonding partners. In contrast, modern MLFFs based on equivariant graph neural networks

cover interactions up to ≈ 15 Å as an ‘all-body’ treatment.

State-of-the-art general-purpose MLFFs, such as SO3LR [13], combine a medium-range many-body description with explicit long-range electrostatic and dispersion terms. This design enables the model to account for interactions beyond short-range effects, improving accuracy for larger systems. Input training data for SO3LR is typically DFT forces, plus Hirshfeld ratios and dipole moments from the same calculations. The larger “effective neighbourhoods” of MLFFs permit the capture of more complex structure from the training data of a wide range of short and medium-range quantum effects such as polarization, charge transfer, and exchange repulsion, which are actively modulated by the local chemical environment. These effects are essential for the accurate modeling of reactive and electronically complex systems. Between the simplified picture of a pure classical MMFF and the immensely more complex parameter space of an MLFF, ‘polarizable’ MMFFs attempt to model the lability of electron distributions, often in a first-order or linearised way, capturing some but not all of the important environment-dependent physics, especially as related to electrostatic moments [14]. MLFFs such as SO3LR mark a substantial improvement over conventional and also polarizable MMFFs by capturing non-local interactions and delicate local electronic effects with high accuracy [15–17].

It is important to recognize that interatomic interactions arising from electronic correlations can be even more farsighted than current MLFFs can describe. For example, atomic interactions in nanoscale systems can span distances of 10–100 nanometers [18–21] and even collective van der Waals interactions between small proteins and water have been shown to exhibit effective decays of 25–30 Å [22]. We leave further investigation of such ultra-long-ranged effects on biomolecular dynamics to future work and here focus on analyzing complex quantum-mechanical effects at short and medium distances.

We begin by validating SO3LR on small molecules through NMA, comparing to the General Amber Force Field 2 (GAFF2) [23]. Vibrational frequencies and their corresponding eigenvectors are benchmarked directly against the DFT references. IR spectra beyond the harmonic approximation are examined to assess the ability of the method to capture anharmonic effects and intensity variations. Building on this foundation, we present a detailed case study of oF-Phe+H⁺, where computed PES of conformer isomers provides mechanistic interpretation of IR spectral features. The scope is then expanded to peptide and protein systems, employing widely used empirical force fields—AMBER [24–26], CHARMM36m [27], OPLS [28], and AMOEBA [29, 30]. Validation is extended to the Alanine-15 peptide, where NMA reveals quantum-level correspondence, highlighting conformational changes driven by energy and entropy. Finally, the p53 transactivation domain is investigated in monomeric and tetrameric forms, both in vacuum and solvated environments, to probe solvent and intraprotein effects on vibrational dynamics. These biologically critical and structurally complex systems are chosen to showcase capture of environmental effects and dynamical couplings by MLFF that are inaccessible to more conventional approaches.

The comprehensive assessment of SO3LR and its applicability across a wide variety of biochemical systems and configurations demonstrates its efficiency, accuracy, scalability, and transferability for the study of biomolecular stability and vibrations compared to high-fidelity quantum reference and experimental data when it is available. This paves the way towards fully predictive molecular dynamics simulations, including intrinsically disordered proteins and antibodies containing non-natural amino acids.

Results and Discussion

PBE0+MBD as an accurate reference method

Density-functional theory (DFT) has become the cornerstone of computational chemistry because it offers a quantum-mechanical description of electronic structure at a fraction of the cost of correlated wavefunction methods [31], such as Coupled Cluster [32] and Quantum Monte Carlo [33]. This balance between accuracy and efficiency makes DFT indispensable for modeling molecular properties, condensed-phase systems, and vibrational spectroscopy. For vibrational frequencies, DFT captures electron correlation and anharmonicity effects sufficiently well to reproduce experimental results, which is essential for predictive modeling [34]. Building on this foundation, the choice of the exchange-correlation functional plays a critical role in determining the accuracy of vibrational properties. Among the many available options, PBE0 stands out as a non-empirical hybrid functional that combines the Perdew–Burke–Ernzerhof (PBE) semi-local functional with exact Hartree–Fock exchange [35, 36]. PBE0 achieves a balanced treatment of semi-local electron exchange and correlation effects, key for the accurate description of vibrational spectroscopy. Benchmark studies show that PBE0 reproduces CCSD(T)-level vibrational frequencies with only small systematic deviations, making it one of the most accurate hybrid functionals for vibrational analysis [37, 38].

Semi-local functionals and pairwise dispersion corrections fail to describe nonadditive many-body dispersion (MBD) effects and long-range electrodynamic screening, which can significantly influence structure, stability, and vibrational properties. The MBD method captures these collective correlations and has been shown to outperform pairwise vdW schemes even in small systems [39, 40]. PBE0+MBD introduces a single empirical parameter—the MBD range separation—while the PBE0 functional itself is fully non-empirical, making this combination both physically grounded and minimally empirical. PBE0+MBD is not, however, entirely without systematic errors and can overestimate charge-transfer contributions in ionic and strongly hydrogen-bonded systems [41, 42].

For biomolecules with localized electronic structure, PBE0+MBD is emerging as an accurate and robust framework [43]. In molecular crystals, PBE0+MBD has been shown to be capable of reproducing experimental IR and Raman spectra, accurately capturing both frequency shifts and intensity patterns [44–47]. In bio-systems, PBE0 parameter-free design and robustness across chemical space make it a reliable choice

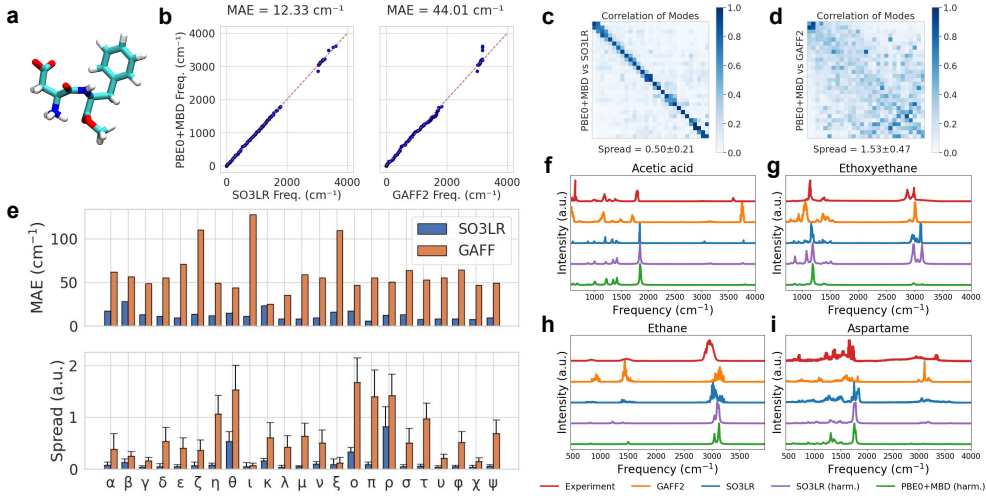


Fig. 1 Vibrational benchmark of SO3LR and GAFF2 using DFT at PBE0+MBD as reference calculation. **a** Aspartame. **b** NMA frequencies of SO3LR (left) and GAFF2 (right) against PBE0+MBD, and MAE based on 1 to 1 fitting. **c–d** Absolute values of correlation matrices of vibrational eigenvectors from SO3LR **c** and GAFF2 **d** versus PBE0+MBD (eq. 1). Spread is reported (eq. 2). For visualisation purposes, a 4x4 max pool filter was applied to the matrix. **e** Whole set comparison of SO3LR (blue) and GAFF2 (orange) versus PBE0+MBD. Error bars represent the standard deviation per molecule. Molecules: 2-Chloroethanol (α), 2-Fluoroethanol (β), 4-Chlorotoluene (γ), Acetic acid (δ), Acetone (ϵ), Acetonitrile (ζ), Acetophenone (η), Aspartame (θ), CO₂ (ι), DMSO (κ), Ethane (λ), Ethanol (μ), Ethoxyethane (ν), Formaldehyde (ξ), Haloperidol (σ), Hexane (π), Ibuprofen (ρ), Methanol (σ), Methylcyclohexane (τ), Phenol (ν), Tetrahydrofuran (ϕ), Toluene (χ) and tert-Butylmercaptan (ψ). **f–i** Comparison of IR spectra versus experiment (red) using GAFF2 (orange) and SO3LR (blue) from dipole autocorrelation and from harmonic approximation SO3LR (purple) and PBE0+MBD (green). Experimental infrared spectra of Acetic acid **f** and Ethoxyethane **g** are extracted from [52, 53]. Ethane **h** and Aspartame **i** are extracted from [54, 55]. Source data are provided as a Source Data File.

for vibrational studies [48, 49]. PBE0+MBD has been successfully applied to peptides and small proteins, recovering experimental spectroscopic observables [50, 51].

Vibrational Landscapes of Small Molecules

As an initial probe of MLFFs as reporters of the molecular vibrational landscape, we employed the SO3LR model [13] trained on PBE0+MBD calculations [35, 36, 39], and assessed its ability to reproduce vibrational properties across a set of small molecules versus MMFF and reference PBE0+MBD calculations. We take PBE0+MBD as the ground truth vibrational reference data since it is known to accurately reproduce CCSD(T) data for small molecules, as we explained in the previous section. In this section the MMFF used was GAFF2 [23]. GAFF2 has transferable bond stretching, angle bending, and torsional parameters which have been developed in an evolutionary way over many years, based on a combination of empirical data and post Hartree-Fock quantum calculations, with semi-empirical AM1-BCC [56] typically used to assign fractional atomic point charges as a per-molecule precalculation step

[57]. The benchmark set was designed as 23 molecules with a diverse range of common functional groups, of which 14 overlap with the SO3LR training set as small species (e.g., CO₂, acetic acid), while more complex molecules such as ibuprofen, haloperidol, and aspartame, are placed in an extrapolation regime and highlight that the benchmark is far from the training distribution. This included flexible scaffolds with multiple rotatable bonds, designed to challenge the force field's ability to capture anharmonic effects and conformation-dependent electron density, and contained seven elements (H, C, O, N, S, F, Cl) common in biological and drug-like molecules.

IR spectroscopy is a widely used technique for probing molecular vibration *via* its coupling to the electric field of light. In MD simulations, these vibrational properties emerge from the interatomic forces defined by the force field. Finite-temperature IR spectra can be computed from the dipole–dipole autocorrelation function obtained from MD trajectories, providing a test of the modelling of dynamics and electrostatics. Unfortunately, the high computational cost of DFT-based MD makes it impractical to use DFT to take *ab initio* IR spectra as a reference. As a cheaper alternative zero-temperature IR spectra can be approximated by harmonic vibrational analysis at optimized minimum-energy geometries (via diagonalisation of a mass-weighted Hessian). The lower cost of MLFFs such as SO3LR and of MMFFs makes it feasible to perform full MD simulations, allowing for a more realistic and dynamic representation of finite temperature vibrational behavior and dipole fluctuations ([§Infrared spectrum](#)). Below we investigate zero-temperature dynamic fluctuations (without calculation of dipole moments or coupling to IR) as NMA and go further where possible, given computational cost to calculate IR spectra at finite temperature and compare these to experiment (Fig. 1).

Two normal mode observables were compared: the zero temperature vibrational frequencies, and the similarity of atomic displacements of each normal mode to those in the DFT results ([§Correlation and Spread Metrics](#)). For aspartame (Fig. 1a), the vibrational frequencies obtained *via* harmonic approximation using SO3LR closely matched the reference, yielding a mean absolute error (MAE) of 12 cm⁻¹. In contrast, GAFF2 displayed a substantially larger deviation, with an MAE of 44 cm⁻¹ (Fig. 1b). The large difference in accuracy is also highlighted in the correlation matrix of normal modes, in which SO3LR reproduces the structural patterns observed in the DFT results (Fig. 1c), whereas GAFF2 does not (Fig. 1d). These observations extend across the entire benchmark set (Fig. 1e). Both the frequency MAE (See Sup. Fig. A1-A2) and the spread scores (See Sup. Fig. A3s-A4) obtained with SO3LR are significantly lower than those of GAFF2 for all tested molecules. A lower spread score indicates a tighter clustering of vibrational mode similarities, suggesting that SO3LR consistently reproduces DFT-like vibrational patterns across diverse molecular systems. These results demonstrate that SO3LR can accurately capture DFT-level vibrational behavior—implicitly learning the Hessian matrix—in a transferable and chemically consistent manner, outperforming MMFFs such as GAFF2 in both accuracy and generalizability even for small molecules.

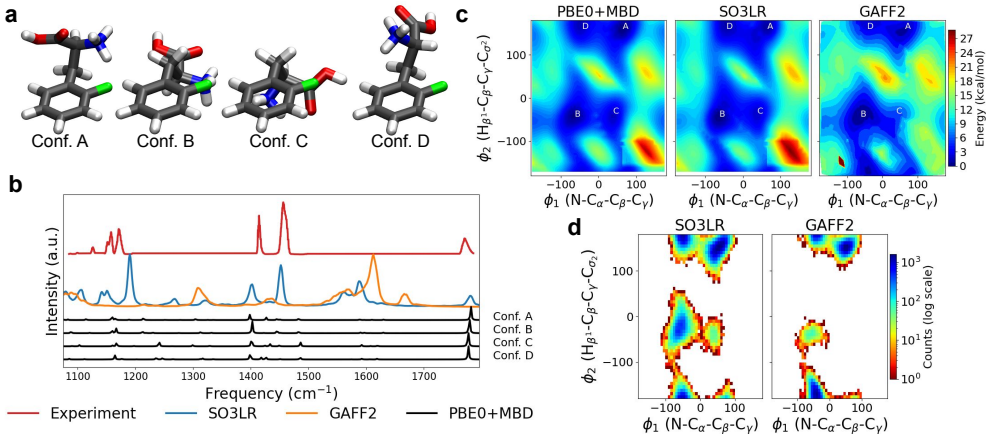


Fig. 2 Vibrational analysis of L-oF-phenylalanine+H⁺. **a** Four stable conformational isomers, ordered from most to least stable, used as initial geometries for harmonic approximation and molecular dynamics simulations. **b** Experimental IR spectrum [58] (red) compared with GAFF2 (orange) and SO3LR (blue) spectra obtained from dipole autocorrelation, alongside harmonic approximation results from PBE0+MBD (black)*. **c** Potential energy surface mapped as a function of ϕ_1 (N-C_α-C_β-C_γ) and ϕ_2 (H_β-C_β-C_γ-C_σ) dihedral angles. Letters indicate conformers defined in panel A. **d** Four independent dihedral sampling during 100 ps simulations initiated from conformer A at 300K. *SO3LR and PBE0+MBD spectrum used a correction factor of 0.966 as in the reference. Source data are provided as a Source Data File.

Trends in the finite-temperature IR are illustrated with acetic acid (Fig. 1f). The MD-derived spectra obtained with SO3LR closely reproduce the frequencies and intensities found at zero-temperature using DFT. For other systems, such as ethoxyethane (Fig. 1g), the predicted intensities show larger deviations, with SO3LR results aligning more closely with experimental IR spectra than with the harmonic DFT calculations, suggesting that finite-temperature effects are captured well. Ethane (Fig. 1h) [54] is a molecule with a rotatable bond, where the inherent anharmonicity of rotational motion (when viewed in Cartesian space) becomes relevant, showing the value of calculating a finite-temperature spectrum using SO3LR and capturing anharmonic effects. In aspartame, another molecule with rotatable bonds (Fig. 1i) [55], SO3LR captures the experimental spectral features with higher accuracy across mid- and high-frequency regions, illustrating the model's ability to describe coupled anharmonic motions in softer and more complex (bio)molecules (See Sup. Fig. A5-A6).

In systems with more conformational freedom, such as L-oF-phenylalanine+H⁺ (oF-Phe+H⁺), even richer behaviour arises. oF-Phe+H⁺ exhibits a wide conformational diversity, driven by strong intramolecular interactions defining 4 stable isomers (Fig. 2a). As shown by M. Safferthal *et al.* [58], the middle-frequency region (1000–2000 cm⁻¹) strongly depends on the balance of these conformational isomers. We therefore investigate the four conformations separately by harmonic approximation at DFT reference level, then further probe the ensemble finite temperature spectrum comparing SO3LR and GAFF2 versus experiment (Fig. 2b). A closer examination of the PES obtained with different methods (Fig. 2c) highlights that SO3LR

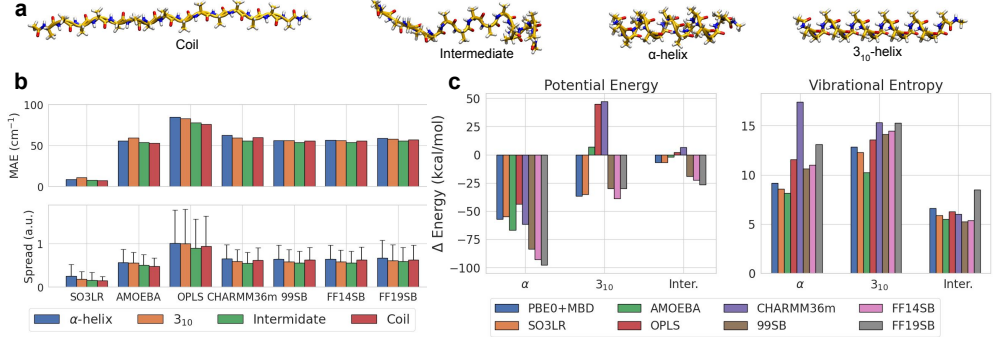


Fig. 3 AceAla₁₅NMe analysis across folding structures. **a** Three-dimensional structures of the four conformers analyzed: canonical α -helix, canonical 3_{10} -helix, intermediate state, and coil (fully extended). **b** Eigenvector and frequency analysis comparing SO3LR and MMFFs to PBE0+MBD. Mean standard error of frequencies and the average spread (see Eq. 2) for the four conformers. Error bars represent standard deviations. **c** Energy differences (kcal mol⁻¹) of the 3_{10} -helix, intermediate state, and coil relative to the α -helix. Potential energy and vibrational entropy contributions ($-TS_{Truhlar}$) are computed using the harmonic approximation at 300K and ν_0 is 50 cm⁻¹. Source data are provided as a Source Data File.

closely reproduces the PBE0+MBD reference data, whereas GAFF2 overestimates conformational barriers and fails to identify conformer C as a local minimum. This discrepancy is further reflected in the 100 ps MD simulations (Fig. 2d): the lower barriers predicted by SO3LR enable extensive conformational sampling between isomers, while the stiffer barriers of GAFF2 hinder such exploration.

SO3LR recovers DFT-like frequency patterns and mode structures across all molecules tested, while GAFF2 exhibits systematic distortions arising from its fixed parametrization. This highlights a central advantage of MLFFs: their ability to reproduce quantum behaviour with chemical specificity and transferability that far exceeds what is achievable with traditional MMFFs.

Stability and Vibrations of AceAla₁₅NMe Peptide

We now extend the study from small molecules to a larger polyalanine, to investigate whether the quantum mechanically accurate behavior of SO3LR observed in small molecules can generalize as molecular size and complexity increase, particularly to systems larger than those in the training dataset. As a case study, we focus on the AceAla₁₅NMe peptide, chosen as a simple but structurally relevant molecule. Its well-characterized folding behavior in vacuum [59, 60] provides a valuable benchmark for evaluating the ability of computational methods to capture secondary structure formation, such as α - and 3_{10} -helices. Once formed, helices can dynamically interconvert between canonical α - and 3_{10} -helical structures. The folding behavior has been successfully reproduced by DFT-based MD simulations [61], many-body potentials [62], as well as by pretrained MLFFs such as GEMS [63], MACE-OFF [64], and SO3LR [13]; here we validate the folding (not captured by MMFF, See Sup. Fig. A7)

to then investigate dynamics in detail.

NMA was performed on four representative snapshots from the folding trajectory (Fig. 3a), with backbone heavy atoms constrained during minimization to prevent structural deviations: (1) a completely unfolded state (coil), (2) an intermediate conformation, (3) a canonical α -helix, and (4) a canonical 3_{10} -helix revealing that SO3LR reproduces the vibrational modes with high fidelity. The six MMFFs tested show significantly lower agreement with DFT (See Sup. Fig. A8-A9). Alignment of modes versus DFT gives a smaller spread for SO3LR compared to the MMFFs (Fig. 3b). Enthalpic stability differences between the canonical α and 3_{10} helix were 20.7 and 19.9 kcal/mol, for DFT and SO3LR, respectively, while MMFFs typically did not capture this equilibrium well, overestimating energy barriers, with values between 53.4 and 108.5 kcal/mol (Fig. 3c). These results confirm explicit DFT+vdW calculations [61], and extend the comparison to NMA dynamical information. The weak performance of MMFFs is attributed at least in part to their (usually) being parameterised in or towards aqueous environments, where the high dielectric response reduces the electrostatic part of the cost for conformational changes, including those electronic-level charge transfer and polarisation effects which are coarse-grained into the MMFF. In a protein structure, however, a given element may be in water or buried: properties across dielectric environments are therefore a fair consideration, thus the systematic overestimation of conformational barriers is likely to persist.

To connect dynamic to thermodynamic differences, vibrational energy decomposition was performed. For both SO3LR and DFT, the vibrational entropy contribution ($-TS_{Truhlar}$) [65] consistently favors the α -helix over the 3_{10} -helix by approximately 4 kcal/mol. For the fully extended coil and intermediate states, the vibrational entropy acts as a stabilizing factor for these conformations, with minimal differences between SO3LR and the reference. Yet, it is the enthalpic term that ultimately drives helical stabilization at 300K [66]. This overall thermodynamic trend is broadly captured by many MMFFs, although the energy discrepancies are generally larger than those observed with MLFF. A notable exception is CHARMM36m, which exhibits substantial deviations in entropic contributions, indicating limitations in treating the vibrational thermodynamics of peptides. The polarizable forcefield AMOEBA captures entropic effects in a way that is relatively quite comparable to the MLFF, suggesting that the ‘softness’ provided by models which include atomic polarization is an important element of the physics governing the entropic balance.

Environment Effects on Vibrations in a Multimeric Protein

We now explore a multimeric protein system to evaluate how SO3LR and MMFFs methodologies capture intermolecular and intramolecular interactions within varying environments in complex biomolecular systems. We investigated the tetrameric DNA-binding domain of p53 (PDB ID: 1SAE), a well-characterized protein known for its structural stability in the tetrameric form. In contrast, its monomeric state is reported to be significantly less stable and prone to unfolding or misfolding [67, 68]. A key question is whether MLFFs trained on small molecules can accurately extrapolate

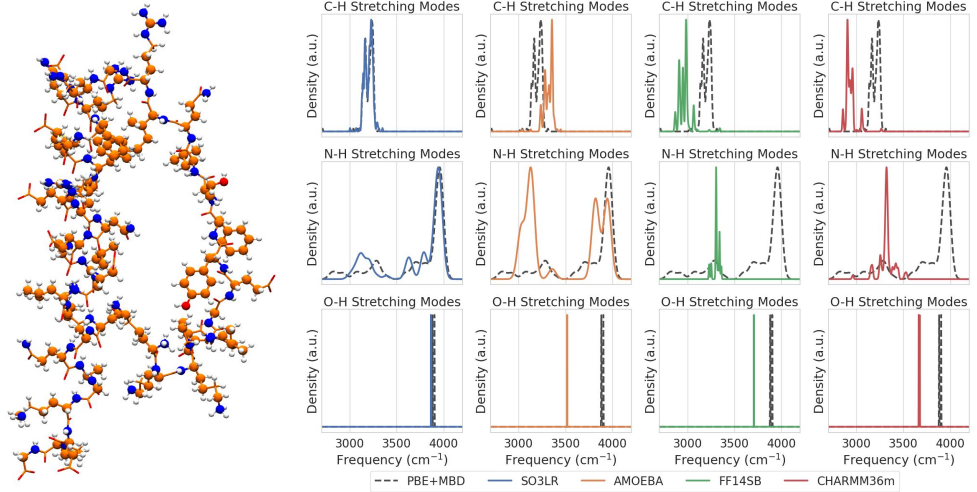


Fig. 4 High frequency stretching modes in p53 monomer. Normalized spectral profiles of C-H, N-H and O-H modes from 2700 to 4200 cm^{-1} in p53 monomer (PDBid: 1SAE) [67]. Different computational methods are shown: PBE+MBD (dotted black), SO3LR (blue), AMOEBA (orange), FF14SB (green) and CHARMM36m (red). Source data are provided as a Source Data File.

and reproduce the behaviour of large biomolecular systems, a bottom-up generalisation challenge. To address this, we performed NMA of the p53 monomer extracted from crystal structures [67] at the PBE+MBD level of theory and compared the resulting vibrational modes with those predicted by SO3LR and MMFF models, since higher-level calculations (PBE0+MBD) were not feasible for this system size.

The MLFF approach again shows promising fidelity with much lower deviations compared to MMFFs (see Sup. Fig. A10). Although SO3LR was not trained on PBE+MBD data, it nevertheless reproduces the reference with notably better accuracy than MMFFs, including in the high-frequency region of the vibrational density of states where some discrepancies remain (see Sup. Fig. A11). When vibrational modes are resolved by chemical identity, SO3LR captures the characteristic C-H, N-H, and O-H stretching distributions far more faithfully than MMFFs (Fig. 4). An intermediate case is the AMOEBA polarizable FF, which captures these stretching modes more accurately than classical MMFFs. These modes are particularly sensitive to fine electronic structure details and anharmonic contributions that classical MMFFs struggle to represent.

We next examined protein–protein interactions specifically focusing on the β -sheet region (residues 227–333) where dimerization of the p53 protein occurs (Fig. 5a, Sup. Fig. A12). The vibrational profile obtained using SO3LR closely matches the reference data from PBE0+MBD, indicating that SO3LR effectively captures the subtle interplay of intra- and intermolecular forces that dominate the dynamics of the dimer interface. In contrast, MMFFs yield significantly different profiles, often failing

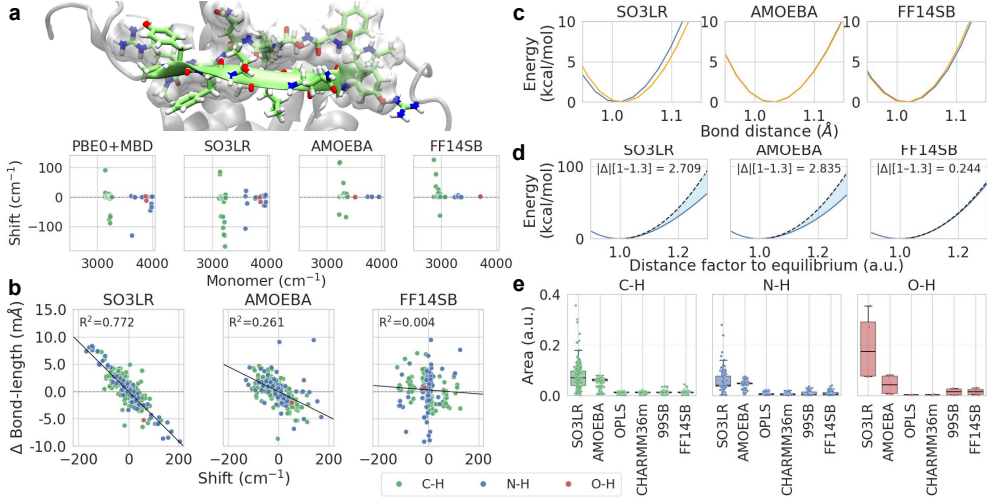


Fig. 5 Environmental effects on stretching modes in p53 multimeric protein. C–H (green), N–H (blue), and O–H (red) stretching modes in the 2700–4200 cm^{−1} region are studied under different conditions. **a** Vibrational shifts between dimer and monomer configurations (x-axis) for the capped fragment of residues 327–333 (green), computed using PBE0+MBD, SO3LR, AMOEBA, and FF14SB. **b** Vibrational shifts plotted against bond-length differences between solvated tetramer and monomer configurations, including the linear correlation R^2 . **c** Potential energy profiles for bond-length perturbations around equilibrium for the N–H stretching mode of the Ile332 backbone, shown for the monomer (blue) and tetramer (orange). **d** Energy comparison for the same atoms as a function of scaled bond distance (0.9–1.3× equilibrium) in the monomer. The shaded region represents the area predicted by a fully harmonic potential from 1.0 to 1.3× the equilibrium distance (dotted). **e** Normalized area distributions (scaled to 1 at maximum) as an anharmonicity measure comparing SO3LR and MMFFs, grouped by bond type. In scatter plots, each point corresponds to the most similar mode matched by the atom index. Source data are provided as a Source Data File.

to reproduce the nuanced packing effects observed in the DFT-level calculations.

In aqueous solution, solvent-dependent shifts arise from a balance of hydrogen-bonding, local electrostatic fields, steric hindrance, and mode coupling. Hydrogen bonding typically elongates and softens O–H and N–H bonds, producing red shifts in their stretching frequencies [69]. Blue shifts can occur in scaffolds exhibiting improper H bonds or when strong local electric fields stiffen the X–H bond—effects showing that electrostatic charge distribution and hydrogen-bond geometry can either red- or blue-shift stretching modes depending on the orientation and nature of the interaction [70, 71].

A comparative analysis of solvation effects in tyrosine, arginine, and leucine, with PBE0+MBD as the reference, shows that SO3LR reliably reproduces solvent-induced vibrational shifts, whereas MMFFs fail to capture these effects (See Supp. Appendix B). For tyrosine, the O–H stretch undergoes a pronounced red shift in both DFT and SO3LR, due to hydrogen bonding of water with the tyrosine hydroxy group, while MMFFs predict minimal change. The N–H groups of arginine exhibit both red and

blue solvent-dependent displacements, which are captured by SO3LR but missed by MMFFs. The C–H stretching modes in all molecules tested show small blue shifts in both SO3LR and DFT, with larger shifts observed in arginine due to the stronger electric fields of its charged groups, while MMFFs yield unrealistic deviations.

Building on these findings, we next examine the p53 protein in a solvated environment, comparing monomeric and tetrameric states to uncover the mechanistic origins of the observed vibrational shifts in a biologically relevant system (see Sup. Fig. A13). Our goal is to determine how these shifts arise from structural adjustments—such as elongation or shortening of X–H bonds—and how they are influenced by the harmonic or anharmonic nature of the vibrational potential. To this end, we compare the N–H, C–H, and O–H stretching frequency shifts with the corresponding bond-length differences between monomer and tetramer, focusing on variations within the range of -10 to $+10$ mÅ (Fig. 5b and Sup. Fig. A14). Remarkably, SO3LR exhibits a clear linear correlation between bond-length changes and vibrational shifts, indicating that the model captures the underlying physical relationship. In contrast, AMOEBA shows only a weak linear trend, while MMFFs fail to reproduce any meaningful correlation.

To illustrate these effects, we examine the N–H stretching mode of the Ile332 backbone amide, which stabilizes the dimerization H-bond with the partner monomer. SO3LR predicts a red shift of 145 cm^{-1} , whereas AMOEBA and FF14SB yield blue shifts of 15 and 45 cm^{-1} , respectively. Inspection of the potential energy profile for bond-length perturbations from 0.9 to 1.3 (Fig. 5c) shows that SO3LR uniquely alters both the equilibrium position and the potential shape due to its environment awareness, while the fixed functional forms of the MMFFs produce nearly identical profiles. Both SO3LR and AMOEBA reproduce an anharmonic bond-stretch profile (Fig. 5d), but the origin of this anharmonicity differs: While SO3LR learns it directly from the QM training data, AMOEBA introduces an analytic anharmonic bond potential [29]. This explains the trend in Fig. 5e, where the normalized area between the fully harmonic and computed potentials is compared: the flexible, environment-responsive SO3LR potential captures DFT-like behavior; AMOEBA’s built-in anharmonicity improves its shifts relative to non-polarizable MMFFs, though its fixed form still limits adaptability.

MMFFs systematically fail to reproduce these behaviours because they lack explicit polarization, many-body induction, anharmonicity, and environment-sensitive hydrogen-bond descriptions. Their harmonic bond potentials and fixed charges cannot capture the solvent-dependent, cooperative stabilization patterns observed in strongly hydrogen-bonded systems. Since bond-stretch anharmonicity is a primary driver of frequency shifts, harmonic force fields predict little change upon stretching; mode coupling can shift frequencies, but this mechanism alone yields incorrect behavior. Accurately reproducing these shifts requires a quantum-mechanical treatment of the dynamical behavior of electrons and anharmonicity. An important exception among MMFFs is AMOEBA, which incorporates explicit polarization, multipole electrostatics, and anharmonic bond terms. These features allow AMOEBA

to capture hydrogen-bond cooperativity and vibrational shifts more faithfully than non-polarizable MMFFs. However, despite its improved physical realism, AMOEBA still relies on fixed functional forms and parameter sets that do not fully capture the changing chemical environments.

Final Remarks

MMFFs remain widely used in biomolecular simulations, yet their reliance on fixed functional forms and empirical fitting limits their ability to capture complex vibrational and environmental effects. Although the AMOEBA polarizable MMFF performs slightly better than MMFFs by incorporating explicit polarization and anharmonic terms, its fixed functional forms still prevent it from fully capturing environment-dependent electronic responses. Accurate modeling of solvent interactions, protein–protein contacts, and conformational flexibility requires approaches that go beyond these constraints. Our results highlight the transformative potential of MLFFs, particularly SO3LR, which is trained on quantum-mechanical data and exhibits a multiscale character capable of reproducing both local and non-local interactions with near-DFT accuracy. SO3LR demonstrates high-fidelity predictions far beyond its training domain, consistently capturing solvent-induced vibrational shifts, protein–protein interaction effects, and subtle coupling patterns inaccessible to MMFFs. This ability to generalize across the vastness of chemical space—from small molecules to multimeric proteins—while maintaining structural and dynamical fidelity marks a significant departure from traditional force fields. MMFFs often fail qualitatively, underestimating solvent effects, misrepresenting intensities, and exaggerating energy barriers. Overall, SO3LR exemplifies a new generation of environment-aware, quantum-accurate force fields that represent a paradigm shift in biomolecular simulation, enabling more accurate, transferable, and physically realistic models for studying molecular dynamics.

Methods

Density-Functional Theory calculations

DFT calculations were performed using the FHI-aims software package (version 221103) [72], employing the PBE0 hybrid exchange-correlation functional [36] combined with the Many-Body Dispersion (MBD) correction scheme to account for long-range van der Waals interactions [39, 73]. For geometry optimizations and energy evaluations, “tight” numerical settings were applied to small organic molecules, “intermediate” settings were used for the larger AceAla₁₅NMe peptide and the Ace- β -sheet-NMe dimer and monomer (residues 327 to 333) of p53 system to balance accuracy and computational cost. Due to the high computational expense, the p53 monomer was computed at the PBE+MBD [35] level of theory using “light” settings.

Molecular dynamics

Classical MMFFs dynamics were performed using OpenMM 8.1.1 [74] with the Langevin middle integrator [75]. In total, seven widely used classical force fields were

evaluated: 99SB-ILDN [24], FF14SB [25], and FF19SB [26] from the AMBER family; CHARMM36m [27]; OPLS-AA [28] and the polarizable AMOEBA force field [29, 30]. Pretrained SO3LR model dynamics were performed using the jax-md [76] package with the Nosé-Hoover integrator [77] for NVT ensembles, and a long-range cut-off of 12 Å.

Normal Mode Analysis

Each molecule was geometry-optimized using different methods depending on the level of theory. For classical MMFF, the L-BFGS algorithm implemented in OpenMM was employed, with a convergence criterion of a maximum force below 1 kJ/nm. For MLFFs, optimization was performed using ASE [78], with a stricter force threshold of 5×10^{-3} eV/Å. DFT calculations were carried out using the BFGS algorithm in FHI-aims, with a convergence criterion of 5×10^{-3} eV/Å.

For the AceAla₁₅NMe peptide, during geometry optimization, the backbone carbon and nitrogen atoms were constrained to preserve the backbone conformation. The p53 monomer and tetramer structures used in calculations were taken directly from the reference structure (PDB ID: 1SAE) [67]. In solvated systems, molecules were optimised with a convergence criteria of 5×10^{-2} eV/Å in the case of SO3LR.

Numerical Hessians were computed using finite displacements: 0.005 Å for classical MMFF, and 0.01 Å for both MLFF and DFT. In the case of multimeric proteins, only the protein atoms were displaced during Hessian construction, while solvent atoms were included in the force evaluations. Normal mode analysis was then performed to extract vibrational eigenvectors and frequencies from the Hessians.

Correlation and Spread Metrics

To evaluate the pair-wise similarity between the vibrational modes derived from two different computational methods, we compute the correlation matrix based on the dot product between their respective eigenvector sets. These eigenvectors are sorted in ascending order according to their associated eigenvalues to ensure a consistent one-to-one comparison of vibrational modes. Let $\mathbf{V}_A \in \mathbb{R}^{n \times n}$ and $\mathbf{V}_B \in \mathbb{R}^{n \times n}$ denote the matrices whose columns are the eigenvectors obtained from Method A and Method B, respectively. The correlation matrix is then defined as:

$$\mathbf{C} = \mathbf{V}_A \cdot \mathbf{V}_B^\top \quad (1)$$

Each element C_{ij} of this matrix represents the dot product between the i -th eigenvector of Method A and the j -th eigenvector of Method B. This provides a direct measure of alignment between the two sets of eigenvectors: values close to 1 or -1 indicate strong alignment (or anti-alignment), while values near 0 signify orthogonality. Because the eigenvectors are ordered according to their eigenvalues, similarity between the vibrational modes obtained from both methods should manifest as strong diagonal dominance in the correlation matrix.

To further quantify the deviation from a perfect one-to-one correspondence between

vibrational modes, we introduce the *spread score* S_i for each mode i :

$$S_i = \sum_{j=1}^N C_{i,j} \frac{|i-j|}{N}, \quad (2)$$

being N the total number of modes, $C_{i,j}$ the value of the correlation matrix at position (i,j) , and $|i-j|/N$ the normalized distance from the diagonal.

As shown in Eq. 2, this score captures how much the correlation of a given mode is distributed across other modes, rather than being sharply peaked at the diagonal. In this way, a low spread score indicates that the correlation is concentrated near the diagonal (i.e., strong mode-to-mode correspondence), while a high score shows poor alignment to the reference data.

Infrared spectrum

20 independent 100 ps NVE trajectories with a 0.1 fs/step were used after 10 ps NVT equilibration. The instantaneous dipole moment of the system was calculated at each step. The dipole moment vector, $\vec{\mu}(t)$, was obtained using the following equation:

$$\vec{\mu}(t) = \sum_i q_i \vec{r}_i(t), \quad (3)$$

where q_i is the charge of the i -th atom and $\vec{r}_i(t)$ is its position at time t . The dipole moment autocorrelation function (ACF) was computed from the time series of dipole moments. The ACF, $C_\mu(t)$, is defined as:

$$C_\mu(t) = \langle \vec{\mu}(0) \cdot \vec{\mu}(t) \rangle. \quad (4)$$

The IR spectrum was obtained by performing a Fourier transform of the dipole moment ACF. The power spectrum, $I(\omega)$, is given by:

$$I(\omega) = \int_{-\infty}^{\infty} C_\mu(t) e^{-i\omega t} dt, \quad (5)$$

where ω is the angular frequency. The final spectrum is obtained by averaging over all trajectories.

PBE0+MBD IR spectra were obtained by harmonic approximation using TheSeuSS package [46].

Potential energy surface

Two dihedral angles of L-oF-phenylalanine+H⁺, ϕ_1 (N-C_α-C_β-C_γ) and ϕ_2 (H_{β1}-C_β-C_γ-C_{σ2}), were selected for torsional analysis. A 10° rotational window was applied, using the most stable conformation as the starting point. For each position, fixed-dihedral minimization was performed with SO3LR and GAFF2. In GAFF2, an

external dihedral constraint of 50 kcal·mol⁻¹ was imposed. For DFT, constrained relaxation was first carried out with ORCA 6.1.1 [79] at the PBE0 level, followed by FHI-aims at PBE0+MBD, where dihedral atom positions were fixed due to the lack of direct dihedral constraints in FHI-aims.

Molecular Visualization

Three-dimensional molecular structures were visualized using VMD version 1.9.4a57 [80].

Data availability

The data generated in this study, including details about computational calculations, simulations and additional performance tests are provided in the Supplementary Information. Source data are provided with this paper.

References

- [1] Hollingsworth, S. A. & Dror, R. O. Molecular dynamics simulation for all. *Neuron* **99**, 1129–1143 (2018).
- [2] Ciccotti, G., Dellago, C., Ferrario, M., Hernández, E. R. & Tuckerman, M. E. Molecular simulations: past, present, and future (a Topical Issue in EPJB). *Eur. Phys. J. B* **95**, 3 (2022).
- [3] Jumper, J. *et al.* Highly accurate protein structure prediction with AlphaFold. *Nature* **596**, 583–589 (2021).
- [4] Chan-Yao-Chong, M., Chan, J. & Kono, H. Benchmarking of force fields to characterize the intrinsically disordered R2-FUS-LC region. *Sci. Rep.* **13**, 14226 (2023).
- [5] Salvi, N., Abyzov, A. & Blackledge, M. Solvent-dependent segmental dynamics in intrinsically disordered proteins. *Sci. Adv.* **5**, eaax2348 (2019).
- [6] Marcellini, M., Nguyen, M.-H., Martin, M., Hologne, M. & Walker, O. Accurate prediction of protein NMR spin relaxation by means of polarizable force fields. application to strongly anisotropic rotational diffusion. *J. Phys. Chem. B* **124**, 5103–5112 (2020).
- [7] Salvi, N. *et al.* Convergent views on disordered protein dynamics from NMR and computational approaches. *Biophys. J.* **121**, 3785–3794 (2022).
- [8] Bolik-Coulon, N. *et al.* Explicit models of motion to understand protein side-chain dynamics. *Phys. Rev. Lett.* **129**, 203001 (2022).

- [9] Love, O. *et al.* Evaluating the accuracy of the AMBER protein force fields in modeling dihydrofolate reductase structures: misbalance in the conformational arrangements of the flexible loop domains. *J. Biomol. Struct. Dyn.* **41**, 5946–5960 (2023).
- [10] Stroet, M. *et al.* On the validation of protein force fields based on structural criteria. *J. Phys. Chem. B* **128**, 4602–4620 (2024).
- [11] Nettels, D. *et al.* Single-molecule fret for probing nanoscale biomolecular dynamics. *Nat. Rev. Phys.* **6**, 587–605 (2024).
- [12] Ditler, E. & Luber, S. Vibrational spectroscopy by means of first-principles molecular dynamics simulations. *WIREs Comput. Mol. Sci.* **12**, e1605 (2022).
- [13] Kabylda, A. *et al.* Molecular simulations with a pretrained neural network and universal pairwise force fields. *J. Am. Chem. Soc.* **147**, 33723–33734 (2025).
- [14] Ren, P. & Ponder, J. W. Polarizable atomic multipole water model for molecular mechanics simulation. *J. Phys. Chem. B* **107**, 5933–5947 (2003).
- [15] Chmiela, S., Sauceda, H. E., Müller, K.-R. & Tkatchenko, A. Towards exact molecular dynamics simulations with machine-learned force fields. *Nat. Commun.* **9**, 3887 (2018).
- [16] Sauceda, H. E., Chmiela, S., Poltavsky, I., Müller, K.-R. & Tkatchenko, A. Molecular force fields with gradient-domain machine learning: Construction and application to dynamics of small molecules with coupled cluster forces. *J. Chem. Phys.* **150**, 114102 (2019).
- [17] Unke, O. T. *et al.* Machine learning force fields. *Chem. Rev.* **121**, 10142–10186 (2021).
- [18] Ambrosetti, A., Ferri, N., DiStasio, R. A. & Tkatchenko, A. Wavelike charge density fluctuations and van der waals interactions at the nanoscale. *Science* **351**, 1171–1176 (2016).
- [19] Hauseux, P. *et al.* From quantum to continuum mechanics in the delamination of atomically-thin layers from substrates. *Nat. Commun.* **11**, 1651 (2020).
- [20] Hauseux, P., Ambrosetti, A., Bordas, S. P. A. & Tkatchenko, A. Colossal enhancement of atomic force response in van der waals materials arising from many-body electronic correlations. *Phys. Rev. Lett.* **128**, 106101 (2022).
- [21] Sosa, R. I., Galante, M. & Tkatchenko, A. Power of the many-body force: Magnitudes and angles of atomic van der waals dispersion forces in extended molecular systems. *Small Struct.* **6**, 2500226 (2025).

- [22] Stöhr, M. & Tkatchenko, A. Quantum mechanics of proteins in explicit water: The role of plasmon-like solute-solvent interactions. *Sci. Adv.* **5**, eaax0024 (2019).
- [23] He, X., Man, V. H., Yang, W., Lee, T. S. & Wang, J. A fast and high-quality charge model for the next generation general AMBER force field. *J. Chem. Phys.* **153**, 114502 (2020).
- [24] Lindorff-Larsen, K. *et al.* Improved side-chain torsion potentials for the amber ff99SB protein force field. *Proteins: Structure, Function, and Bioinformatics* **78**, 1950–1958 (2010).
- [25] Maier, J. A. *et al.* ff14SB: Improving the accuracy of protein side chain and backbone parameters from ff99SB. *J. Chem. Theory Comput.* **11**, 3696–3713 (2015).
- [26] Tian, C. *et al.* ff19SB: Amino-acid-specific protein backbone parameters trained against quantum mechanics energy surfaces in solution. *J. Chem. Theory Comput.* **16**, 528–552 (2020).
- [27] Huang, J. *et al.* CHARMM36m: an improved force field for folded and intrinsically disordered proteins. *Nat. Methods* **14**, 71–73 (2017).
- [28] Robertson, M. J., Tirado-Rives, J. & Jorgensen, W. L. Improved peptide and protein torsional energetics with the OPLS-AA force field. *J. Chem. Theory Comput.* **11**, 3499–3509 (2015).
- [29] Shi, Y. *et al.* Polarizable atomic multipole-based AMOEBA force field for proteins. *J. Chem. Theory Comput.* **9**, 4046–4063 (2013).
- [30] Zhang, C. *et al.* AMOEBA polarizable atomic multipole force field for nucleic acids. *J. Chem. Theory Comput.* **14**, 2084–2108 (2018).
- [31] Jones, R. O. Density functional theory: Its origins, rise to prominence, and future. *Rev. Mod. Phys.* **87**, 897–923 (2015).
- [32] Bartlett, R. J. & Musiał, M. Coupled-cluster theory in quantum chemistry. *Rev. Mod. Phys.* **79**, 291–352 (2007).
- [33] Austin, B. M., Zubarev, D. Y. & Lester, W. A. J. Quantum monte carlo and related approaches. *Chem. Rev.* **112**, 263–288 (2012).
- [34] Hanson-Heine, M. W. D. Static electron correlation in anharmonic molecular vibrations: A hybrid tao-dft study. *J. Phys. Chem. A* **126**, 7273–7282 (2022).
- [35] Perdew, J. P., Ernzerhof, M. & Burke, K. Rationale for mixing exact exchange with density functional approximations. *J. Chem. Phys.* **105**, 9982–9985 (1996).

- [36] Adamo, C. & Barone, V. Toward reliable density functional methods without adjustable parameters: The PBE0 model. *J. Chem. Phys.* **110**, 6158–6170 (1999).
- [37] Nandi, A. *et al.* Δ -machine learning to elevate DFT-based potentials and a force field to the CCSD(T) level illustrated for ethanol. *J. Chem. Theory Comput.* **20**, 8807–8819 (2024).
- [38] Gleeson, R., Aggelund, P. A., Østergaard, F. C., Schatz, K. F. & Sauer, S. P. A. Exploring alternate methods for the calculation of high-level vibrational corrections of NMR spin–spin coupling constants. *J. Chem. Theory Comput.* **20**, 1228–1243 (2024).
- [39] Tkatchenko, A., DiStasio, R. A., Car, R. & Scheffler, M. Accurate and efficient method for many-body van der Waals interactions. *Phys. Rev. Lett.* **108**, 236402 (2012).
- [40] DiStasio, R. A., Gobre, V. V. & Tkatchenko, A. Many-body van der Waals interactions in molecules and condensed matter. *J. Phys.: Condens. Matter* **26**, 213202 (2014).
- [41] Hermann, J. & Tkatchenko, A. Density functional model for van der Waals interactions: Unifying many-body atomic approaches with nonlocal functionals. *Phys. Rev. Lett.* **124**, 146401 (2020).
- [42] Nickerson, C. J., Bryenton, K. R., Price, A. J. A. & Johnson, E. R. Comparison of density-functional theory dispersion corrections for the DES15K database. *J. Phys. Chem. A* **127**, 8712–8722 (2023).
- [43] Puleva, M. *et al.* Extending quantum-mechanical benchmark accuracy to biological ligand-pocket interactions. *Nat. Commun.* **16**, 8583 (2025).
- [44] Hoja, J. *et al.* Reliable and practical computational description of molecular crystal polymorphs. *Sci. Adv.* **5** (2019).
- [45] Hoja, J., List, A. & Boese, A. D. Multimer embedding approach for molecular crystals up to harmonic vibrational properties. *J. Chem. Theory Comput.* **20**, 357–367 (2024).
- [46] Boziki, A., Mebenga, F. N., Fernandes, P. & Tkatchenko, A. A journey with THeSeuSS: Automated python tool for modeling ir and raman vibrational spectra of molecules and solids. *WIREs Comput. Mol. Sci.* **15**, e70033 (2025).
- [47] Hunnisett, L. M. *et al.* The seventh blind test of crystal structure prediction: structure ranking methods. *Acta Crystallogr. Sect. B* **80**, 548–574 (2024).
- [48] Pietropolli Charmet, A. & Cornaton, Y. Benchmarking fully analytic dft force fields for vibrational spectroscopy: A study on halogenated compounds. *J. Mol.*

Struct. 1160, 455–462 (2018).

- [49] Benkyi, I., Tapavicza, E., Fliegl, H. & Sundholm, D. Calculation of vibrationally resolved absorption spectra of acenes and pyrene. *Phys. Chem. Chem. Phys.* **21**, 21094–21103 (2019).
- [50] Rossi, M., Chutia, S., Scheffler, M. & Blum, V. Validation challenge of density-functional theory for peptides—example of Ac-Phe-Ala5-LysH+. *J. Phys. Chem. A* **118**, 7349–7359 (2014).
- [51] Schubert, F. *et al.* Exploring the conformational preferences of 20-residue peptides in isolation: Ac-Ala 19 -Lys + H + vs. Ac-Lys-Ala 19 + H + and the current reach of dft. *Phys. Chem. Chem. Phys.* **17**, 7373–7385 (2015).
- [52] Kochanov, R. *et al.* Infrared absorption cross-sections in HITRAN2016 and beyond: Expansion for climate, environment, and atmospheric applications. *J. Quant. Spectrosc. Radiat. Transf.* **230**, 172–221 (2019).
- [53] Gordon, I. E. *et al.* The HITRAN2020 molecular spectroscopic database. *J. Quant. Spectrosc. Radiat. Transf.* **277**, 107949 (2022).
- [54] of Standards, N. I. & Technology. Nist chemistry webbook, nist standard reference database number 69. [10.18434/T4D303](https://doi.org/10.18434/T4D303) (2025).
- [55] ChemicalBook. IR spectrum for L-alpha-aspartyl-L-phenylalanine 1-metyl ester (22839-47-0) IR2. URL https://www.chemicalbook.com/SpectrumEN_22839-47-0_IR2.htm. Accessed: 2025-04-15.
- [56] Jakalian, A., Jack, D. B. & Bayly, C. I. Fast, efficient generation of high-quality atomic charges. AM1-BCC model: II. parameterization and validation. *J. Comput. Chem.* **23**, 1623–1641 (2002).
- [57] Wang, J., Wolf, R. M., Caldwell, J. W., Kollman, P. A. & Case, D. A. Development and testing of a general amber force field. *J. Comput. Chem.* **25**, 1157–1174 (2004).
- [58] Safferthal, M. *et al.* Cryogenic infrared spectroscopy reveals remarkably short NH+⋯F hydrogen bonds in fluorinated phenylalanines. *Phys. Chem. Chem. Phys.* **25**, 24783–24788 (2023).
- [59] Millhauser, G. L., Stenland, C. J., Hanson, P., Bolin, K. A. & van de Ven, F. J. Estimating the relative populations of 310-helix and α -helix in ala-rich peptides: a hydrogen exchange and high field NMR study. *J. Mol. Biol.* **267**, 963–974 (1997).
- [60] Topol, I. A. *et al.* α - and 3 10 -helix interconversion: A quantum-chemical study on polyalanine systems in the gas phase and in aqueous solvent. *J. Am. Chem. Soc.* **123**, 6054–6060 (2001).

[61] Tkatchenko, A., Rossi, M., Blum, V., Ireta, J. & Scheffler, M. Unraveling the stability of polypeptide helices: Critical role of van der waals interactions. *Phys. Rev. Lett.* **106**, 118102 (2011).

[62] Zhou, R., Bull-Vulpe, E. F., Pan, Y. & Paesani, F. Toward chemical accuracy in biomolecular simulations through data-driven many-body potentials: I. polyalanine in the gas phase. *J. Chem. Theory Comput.* **21**, 6194–6212 (2025).

[63] Unke, O. T. *et al.* Biomolecular dynamics with machine-learned quantum-mechanical force fields trained on diverse chemical fragments. *Sci. Adv.* **10**, eadn4397 (2024).

[64] Kovács, D. P. *et al.* MACE-OFF: Short-range transferable machine learning force fields for organic molecules. *J. Am. Chem. Soc.* **147**, 17598–17611 (2025).

[65] Ribeiro, R. F., Marenich, A. V., Cramer, C. J. & Truhlar, D. G. Use of solution-phase vibrational frequencies in continuum models for the free energy of solvation. *J. Phys. Chem. B* **115**, 14556–14562 (2011).

[66] Rossi, M., Scheffler, M. & Blum, V. Impact of vibrational entropy on the stability of unsolvated peptide helices with increasing length. *J. Phys. Chem. B* **117**, 5574–5584 (2013).

[67] Clore, G. M. *et al.* Refined solution structure of the oligomerization domain of the tumour suppressor p53. *Nat. Struct. Mol. Biol.* **2**, 321–333 (1995).

[68] Gunasekaran, K., Tsai, C.-J. & Nussinov, R. Analysis of ordered and disordered protein complexes reveals structural features discriminating between stable and unstable monomers. *J. Mol. Biol.* **341**, 1327–1341 (2004).

[69] Brünig, F. N., Geburtig, O., von Canal, A., Kappler, J. & Netz, R. R. Time-Dependent Friction Effects on Vibrational Infrared Frequencies and Line Shapes of Liquid Water. *J. Phys. Chem. B* **126**, 1579–1589 (2022).

[70] Selvam, L., Chen, F. & Wang, F. Solvent effects on blue shifted improper hydrogen bond of C–H···O in deoxycytidine isomers. *Chemical Physics Letters* **500**, 327–333 (2010).

[71] Kirsh, J. M. & Kozuch, J. Hydrogen Bond Blueshifts in Nitrile Vibrational Spectra Are Dictated by Hydrogen Bond Geometry and Dynamics. *J. Am. Chem. Soc. Au* **4**, 4844–4855 (2024).

[72] Blum, V. *et al.* Ab initio molecular simulations with numeric atom-centered orbitals. *Comput. Phys. Commun.* **180**, 2175–2196 (2009).

[73] Ambrosetti, A., Reilly, A. M., DiStasio, J., Robert A. & Tkatchenko, A. Long-range correlation energy calculated from coupled atomic response functions. *J.*

Chem. Phys. **140**, 18A508 (2014).

- [74] Eastman, P. *et al.* OpenMM 8: Molecular dynamics simulation with machine learning potentials. *J. Phys. Chem. B* **128**, 109–116 (2024).
- [75] Zhang, Z., Liu, X., Yan, K., Tuckerman, M. E. & Liu, J. Unified efficient thermostat scheme for the canonical ensemble with holonomic or isokinetic constraints via molecular dynamics. *J. Phys. Chem. A* **123**, 6056–6079 (2019).
- [76] Schoenholz, S. S. & Cubuk, E. D. JAX M.D. a framework for differentiable physics (2020). URL <https://github.com/jax-md/jax-md>.
- [77] Tuckerman, M. E., Alejandre, J., López-Rendón, R., Jochim, A. L. & Martyna, G. J. A liouville-operator derived measure-preserving integrator for molecular dynamics simulations in the isothermal–isobaric ensemble. *J. Phys. A Math. Gen.* **39**, 5629 (2006).
- [78] Larsen, A. H. *et al.* The atomic simulation environment—a python library for working with atoms. *J. Phys. Condens. Matter* **29**, 273002 (2017).
- [79] Neese, F. Software update: The ORCA program system—version 6.0. *Wiley Interdiscip. Rev. Comput. Mol. Sci.* **15**, e70019 (2025).
- [80] Humphrey, W., Dalke, A. & Schulten, K. VMD – Visual Molecular Dynamics. *J. Mol. Graph.* **14**, 33–38 (1996).

Acknowledgements

The authors express their gratitude to Ariadni Boziki for the technical support for IR spectrum and numerical Hessian production. Also, to Adil Kabylda and Tobias Henkes for support in MD preparation. S.S.D, F.N.B. and A.T. acknowledge support from the Luxembourg National Research Fund under grant FNR-CORE MBD-in-BMD (18093472) and the European Research Council under ERC-AdG grant FITMOL (101054629). M.G. from the European Union’s Horizon Europe Marie Skłodowska-Curie Actions (MSCA) Postdoctoral Fellowship (101202630). K.H and J.T.B. acknowledge support from the FNR (C20/MS/14588607). The computations were performed on the Luxembourg national supercomputer MeluXina and in the Uni.lu.

Author Contributions

S.S.D. and A.T. designed the research. S.S.D. performed all simulations, carried out data analysis, and wrote the manuscript with input from all the authors. M.G., K.H and F.N.B. provided technical support and scientific discussion throughout the study. J.T.B. and A.T. contributed to the interpretation of the results and the revision of the

manuscript. All authors have read and approved the final version of the manuscript. A.T. supervised the project and guided the scientific discussions.

Competing interests

The authors declare no competing interests.

Additional Information

Supplementary information

The following files are available free of charge.

- SI.pdf:
 - Appendix A: Supplementary Figures A1-A14
 - Appendix B: Amino Acids under Solvent Effects (Figures B1-B3)

Correspondence

Correspondence and requests for materials should be addressed to Alexandre Tkatchenko.

Supplementary information: Stability and
Vibrations of Proteins in Vacuum and Water:
Bridging Quantum Accuracy with Force-Field
Efficiency

Sergio Suárez-Dou¹, Miguel Gallegos¹, Kyunghoon Han¹,
Florian N. Brünig¹, Joshua T. Berryman¹,
Alexandre Tkatchenko^{1*}

¹Department of Physics and Materials Science, University of
Luxembourg, L-1511 Luxembourg City, Luxembourg.

Appendix A Supplementary Figures 1-14

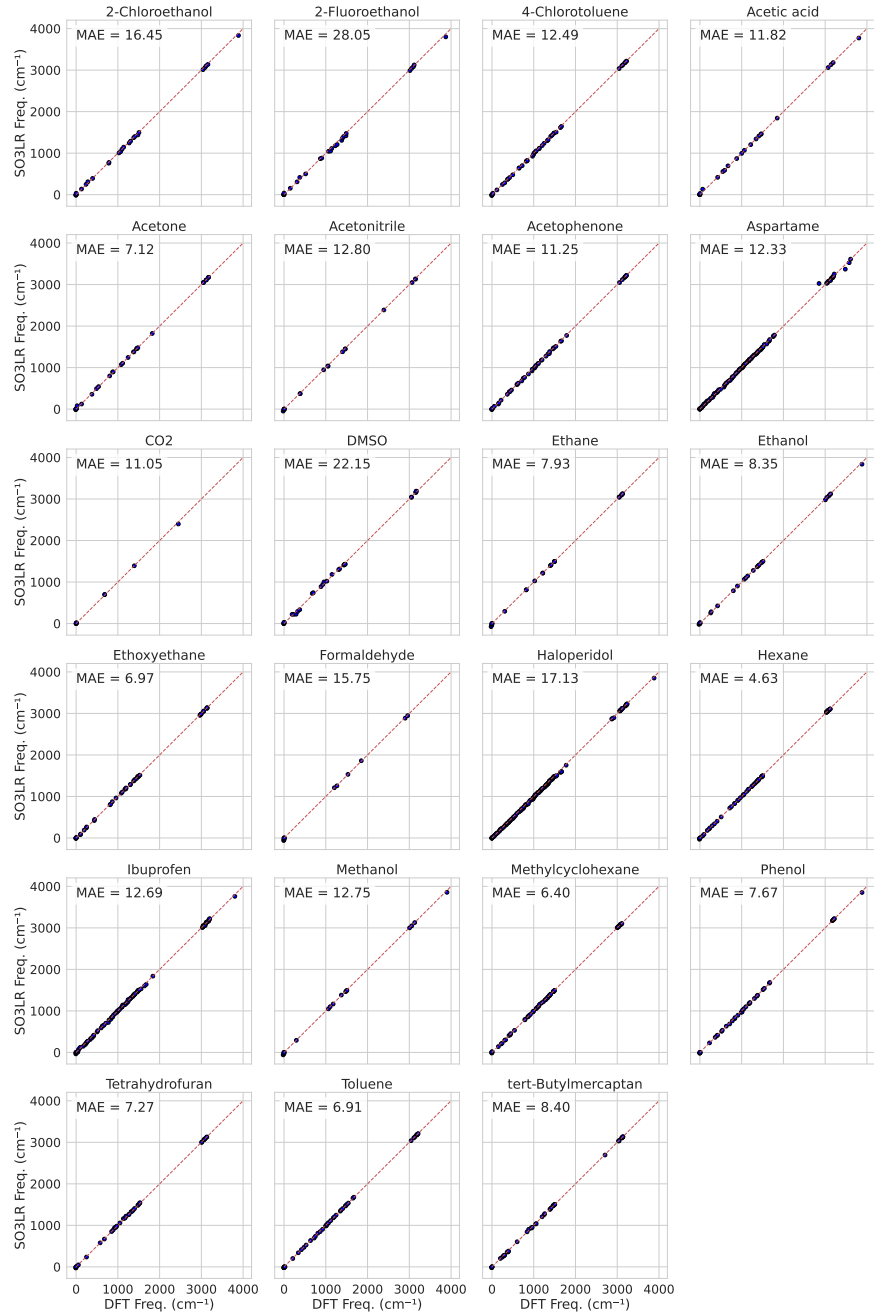


Fig. A1 Vibrational analysis of 23 molecules. Frequency distribution (cm^{-1}) of normal mode analysis of SO3LR against DFT at PBE0+MBD level as reference. Mean absolute error (MAE) from 1 to 1 fitting is shown.

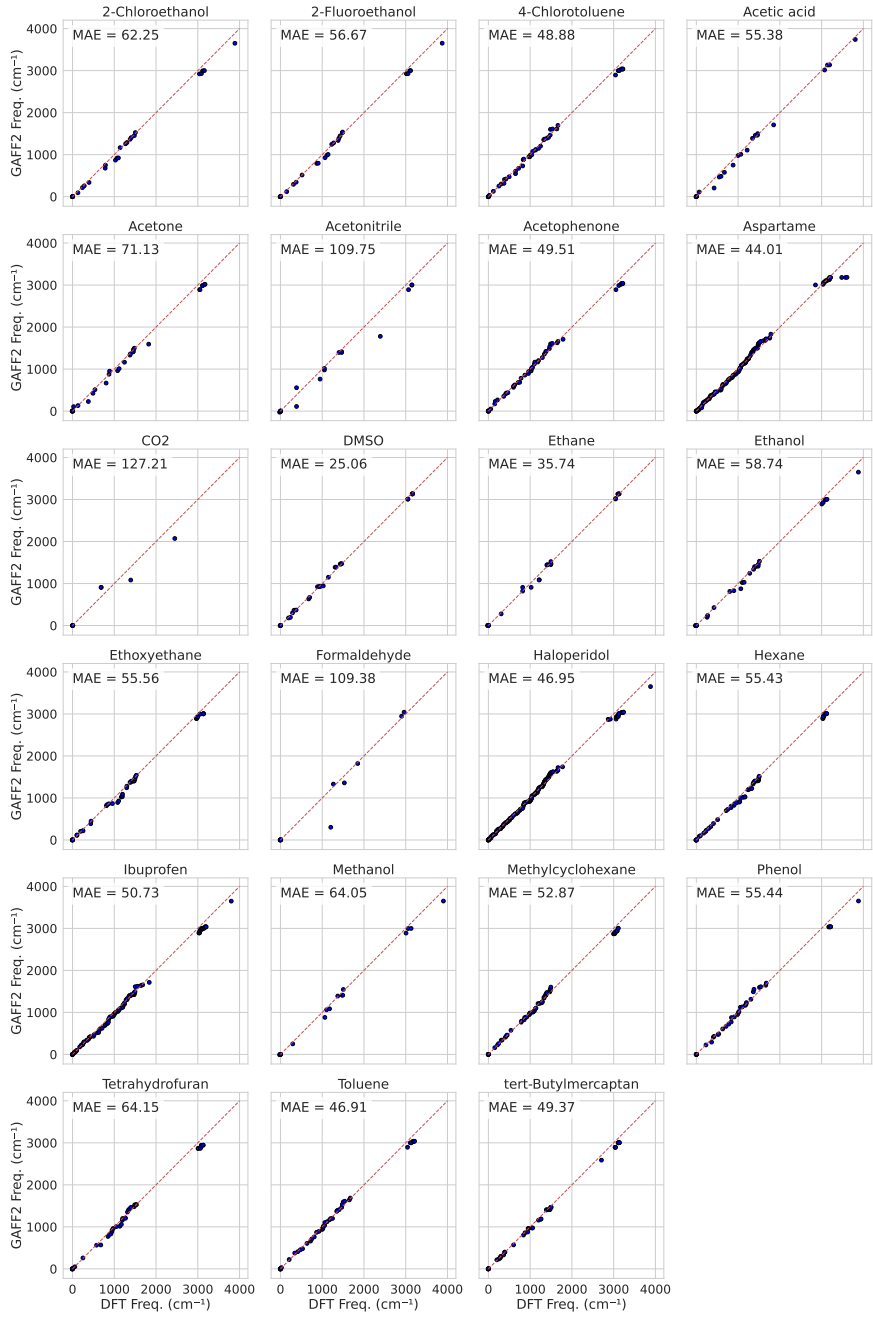


Fig. A2 Vibrational analysis of 23 molecules. Frequency distribution (cm^{-1}) of normal mode analysis of GAFF2 against DFT at PBE0+MBD level as reference. Mean absolute error (MAE) from 1 to 1 fitting is shown.

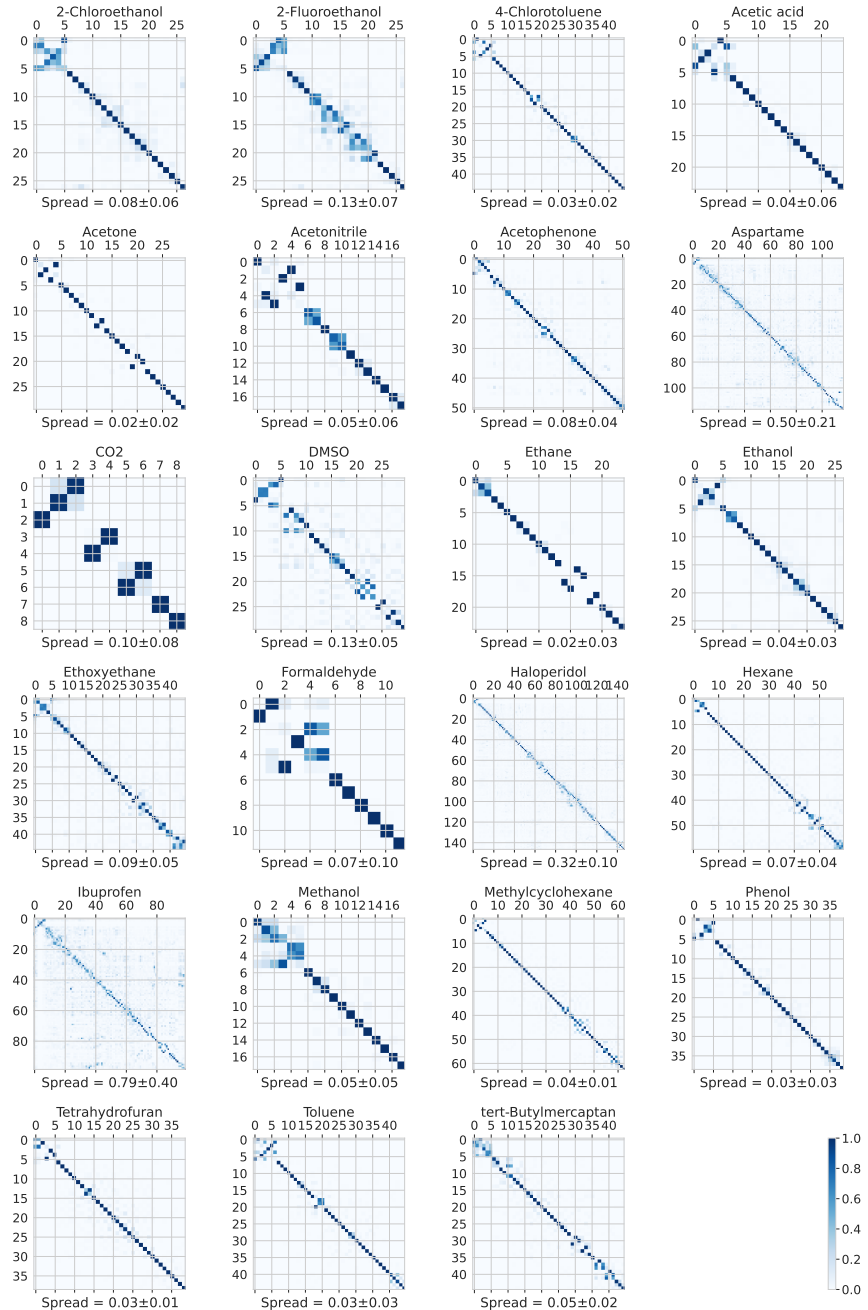


Fig. A3 Correlation matrices comparing the vibrational eigenvectors of 23 different organic molecules from SO3LR with those from DFT at PBE0+MBD level. Absolute values of the correlation coefficients are shown. The normalized spread is reported in each subplot as the mean \pm standard deviation, quantifying the variability of the overlap.

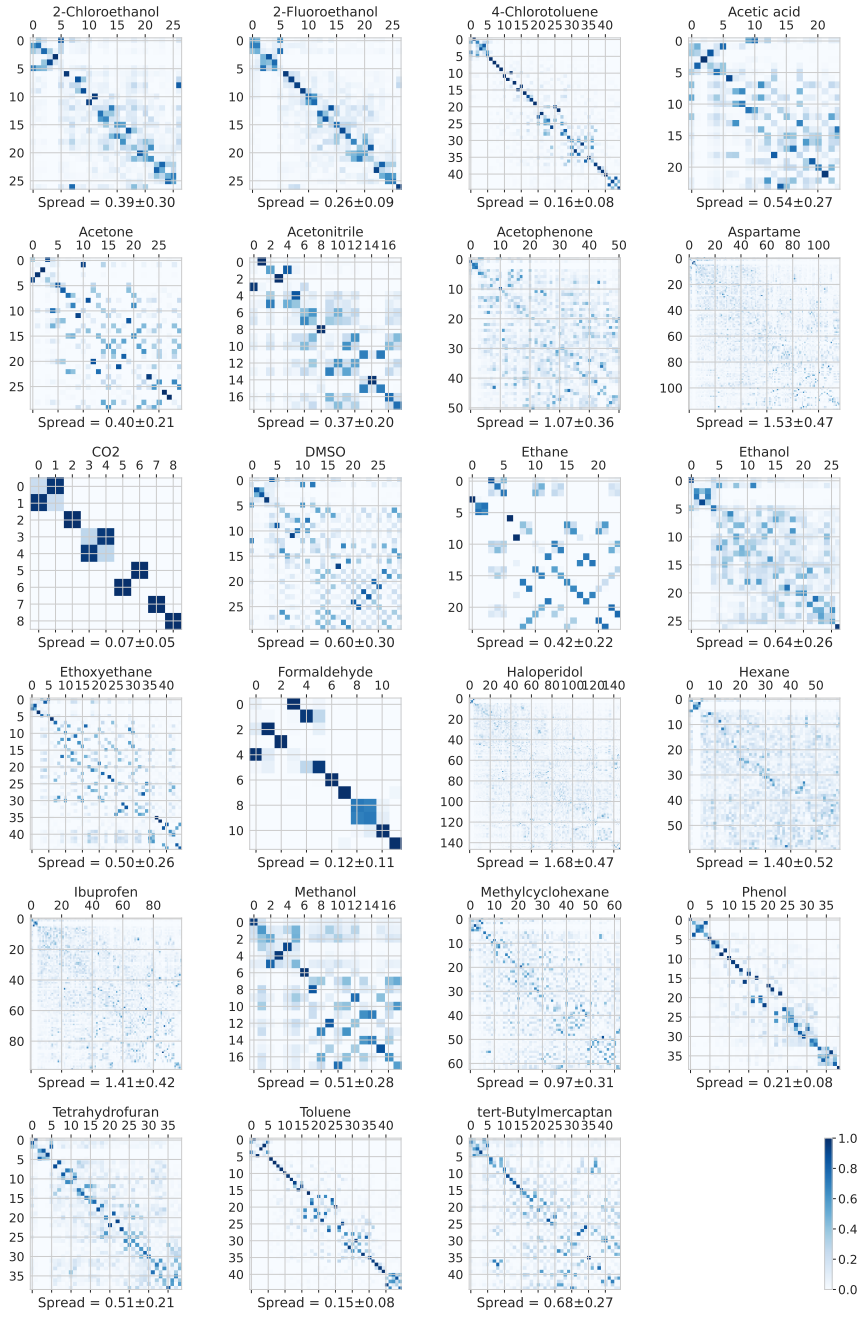


Fig. A4 Correlation matrices comparing the vibrational eigenvectors of 23 different organic molecules from GAFF2 with those from DFT at PBE0+MBD level. Absolute values of the correlation coefficients are shown. The normalized spread is reported in each subplot as the mean \pm standard deviation, quantifying the variability of the overlap.

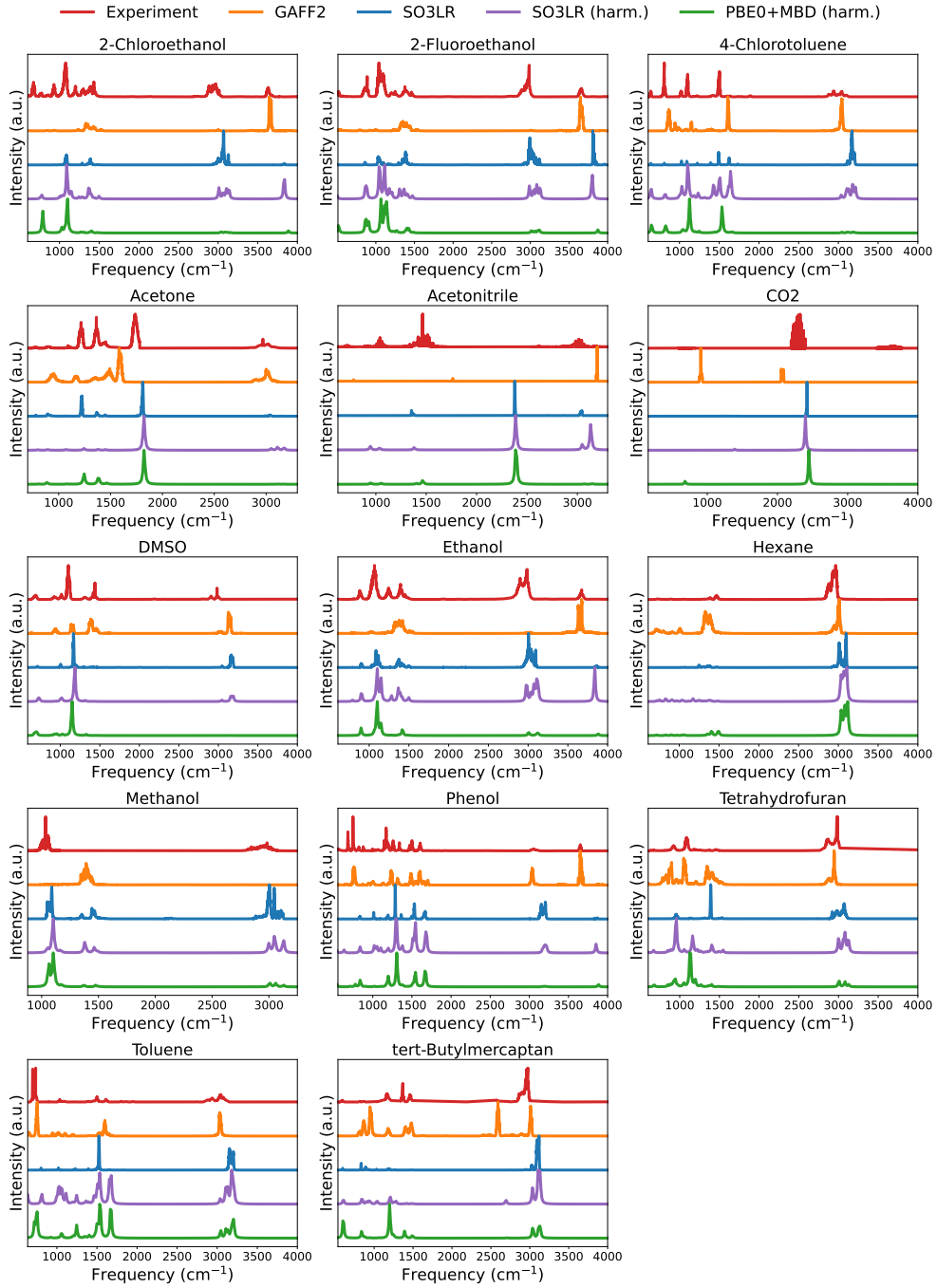


Fig. A5 Infrared spectrum from HITRAN molecules. Experimental values [1, 2] (red), using GAFF2 (orange) and SO3LR (blue) from dipole autocorrelation and from harmonic approximation SO3LR (purple) and DFT at PBE0+MBD (green).

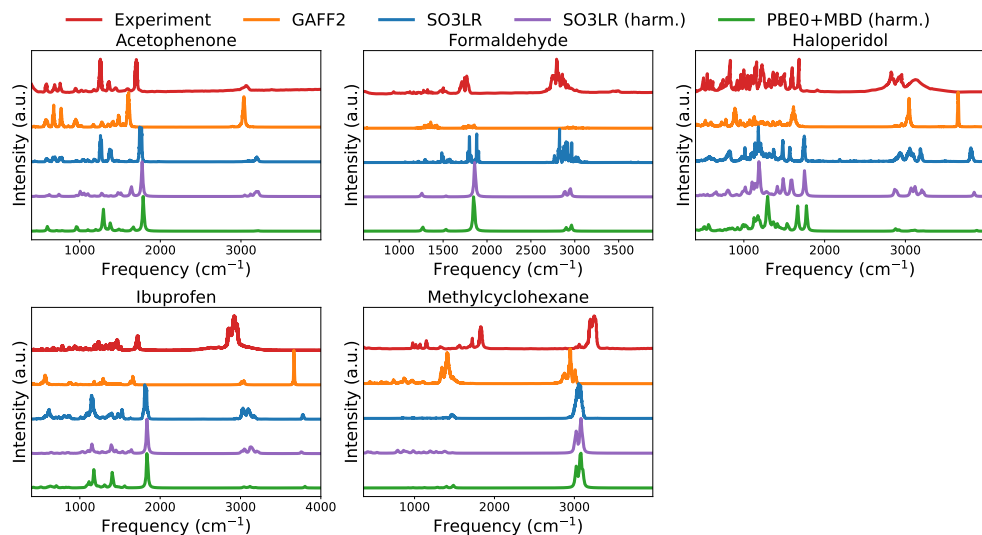


Fig. A6 Infrared spectrum of small molecules. Experimental values (red), using GAFF2 (orange) and SO3LR (blue) from dipole autocorrelation and from harmonic approximation SO3LR (purple) and DFT at PBE0+MBD (green) Experimental values were obtained for Haloperidol, Ibuprofen and Methylcyclohexane from chemicalbook.com. For Acetophenone, and Formaldehyde, were taken from NIST Chemistry WebBook [3].

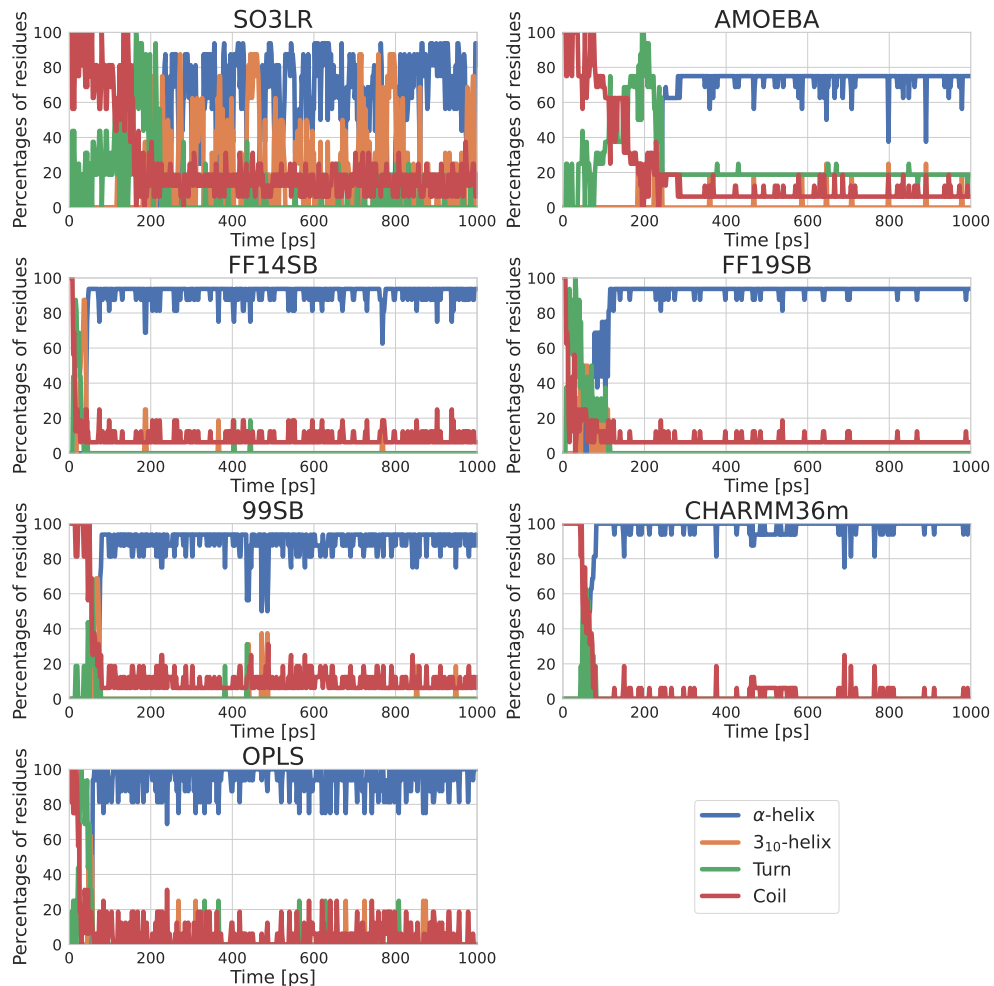


Fig. A7 AceAla15NMe peptide folding path of different FF from complete extended peptide to helical folding during 1 ns of trajectory. Secondary structure was computed with STRIDE [4].

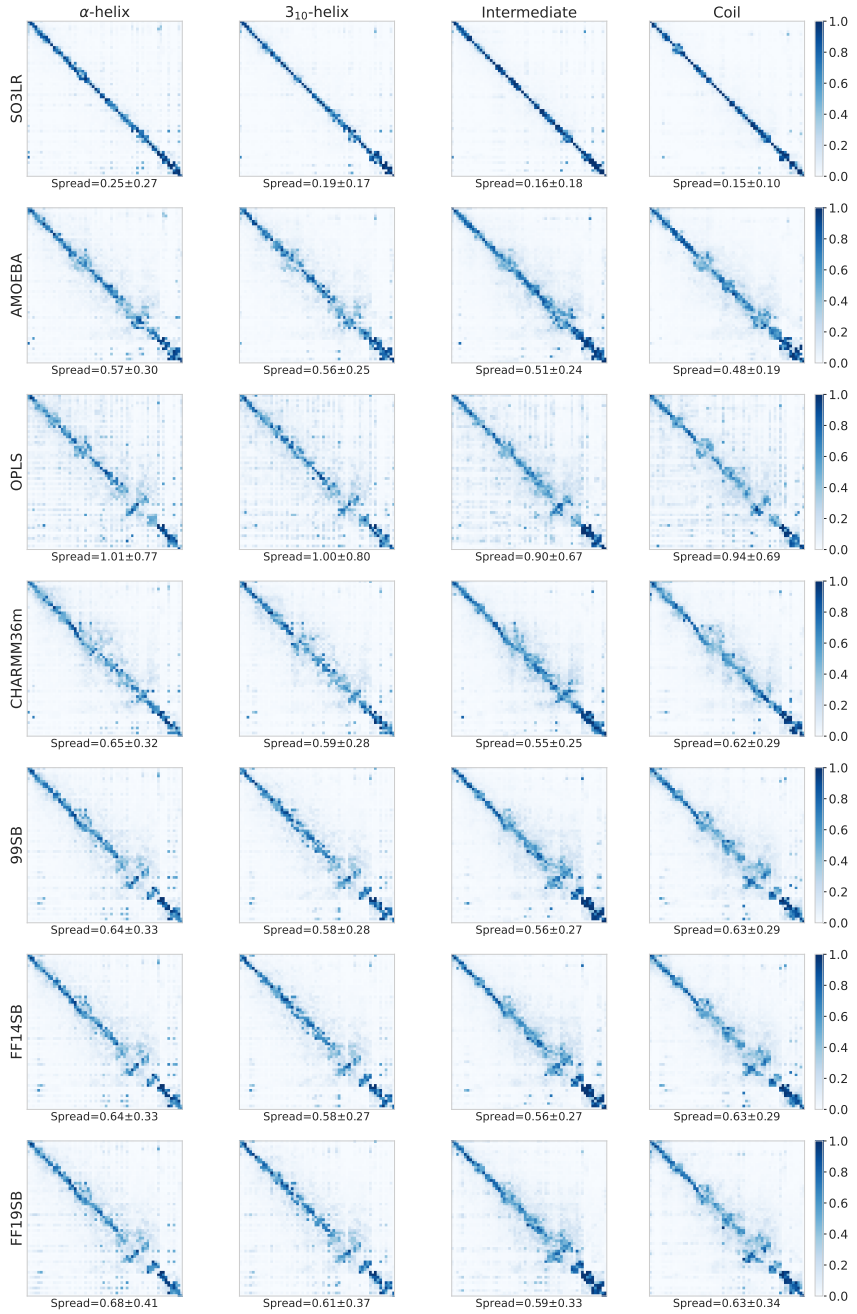


Fig. A8 Correlation matrices comparing the vibrational eigenvectors of AceAla15Nme peptide in 4 different conformation canonical α -helix, canonical 3_{10} -helix, intermediate state and fully extended (coil). SO3LR and 6 different FFs eigenvectors were compared to those from DFT at PBE0+MBD level. Absolute values of the correlation coefficients are shown. For visualization purposes, an 8x8 max pool filter was used to reduce the matrix size. The normalized spread is reported in each subplot as the mean \pm standard deviation.

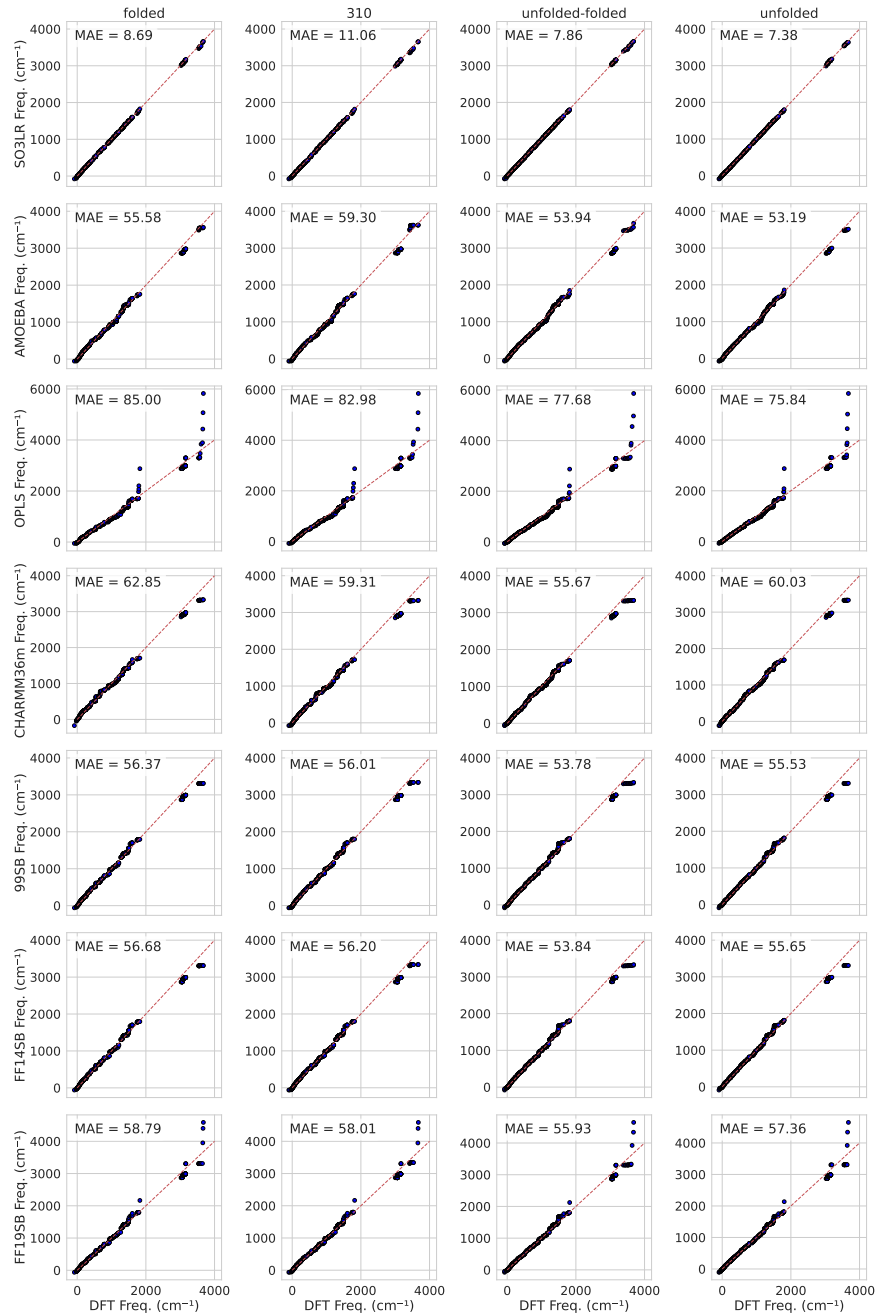


Fig. A9 Vibrational frequency analysis of AceAla15Nme peptide in 4 different conformation canonical α -helix, canonical 3₁₀-helix, intermediate state and fully extended (coil). SO3LR and 6 different FFs frequencies were compared to those from DFT at PBE0+MBD level. Mean absolute error (MAE) from 1 to 1 fitting is shown.

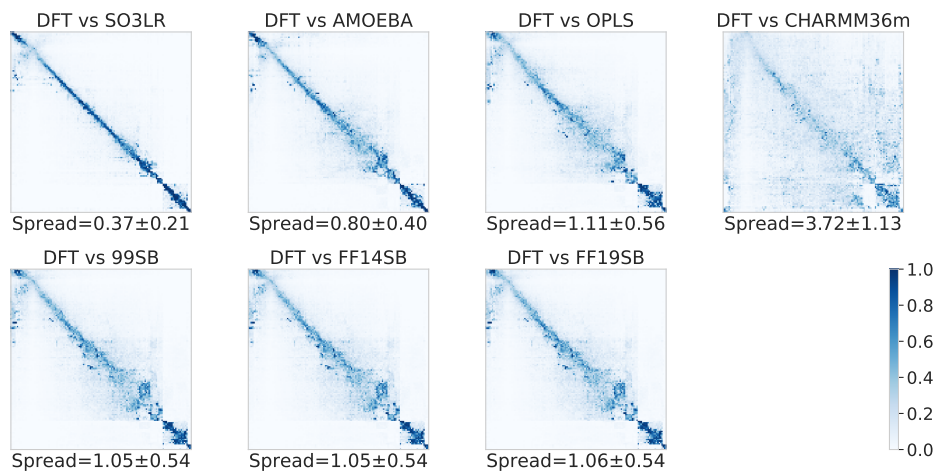


Fig. A10 Correlation matrices comparing the vibrational eigenvectors of p53 monomer. SO3LR and 6 different FFs eigenvectors were compared to those from DFT at PBE+MBD level. Absolute values of the correlation coefficients are shown. For visualization purposes, a 16x16 max pool filter was used to reduce the matrix size. The normalized spread is reported in each subplot as the mean \pm standard deviation.

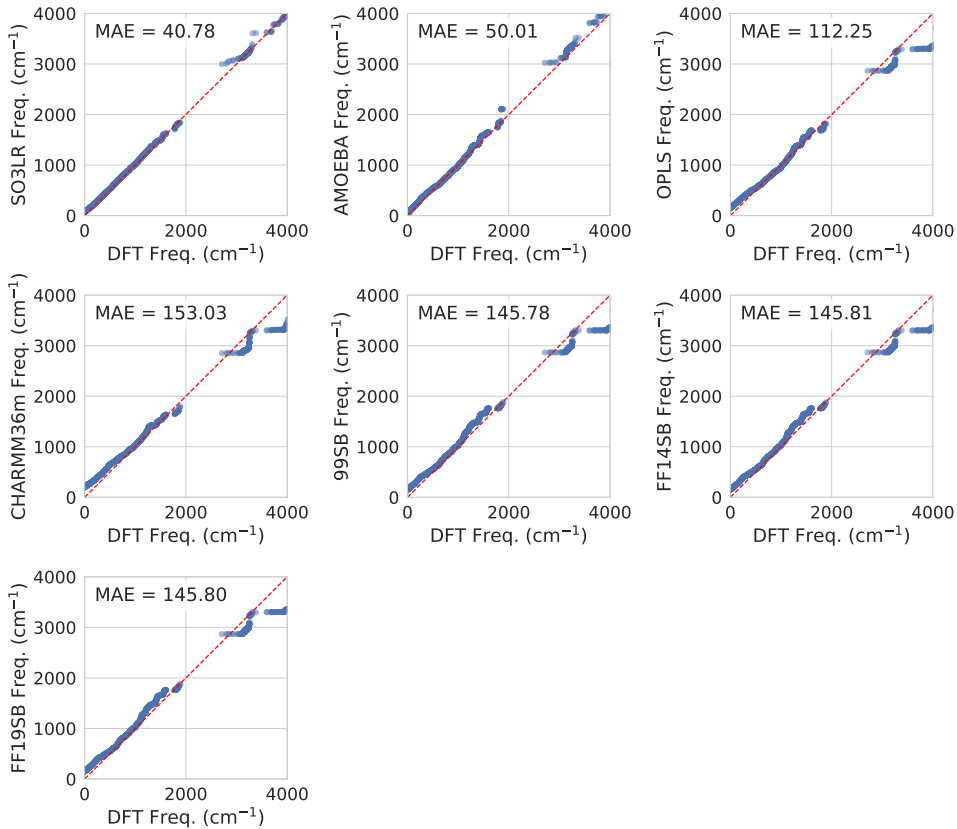


Fig. A11 Vibrational frequency analysis of p53 monomer. SO3LR and 6 different FFs frequencies were compared to those from DFT at PBE+MBD level. Mean absolute error (MAE) from 1 to 1 fitting is shown.

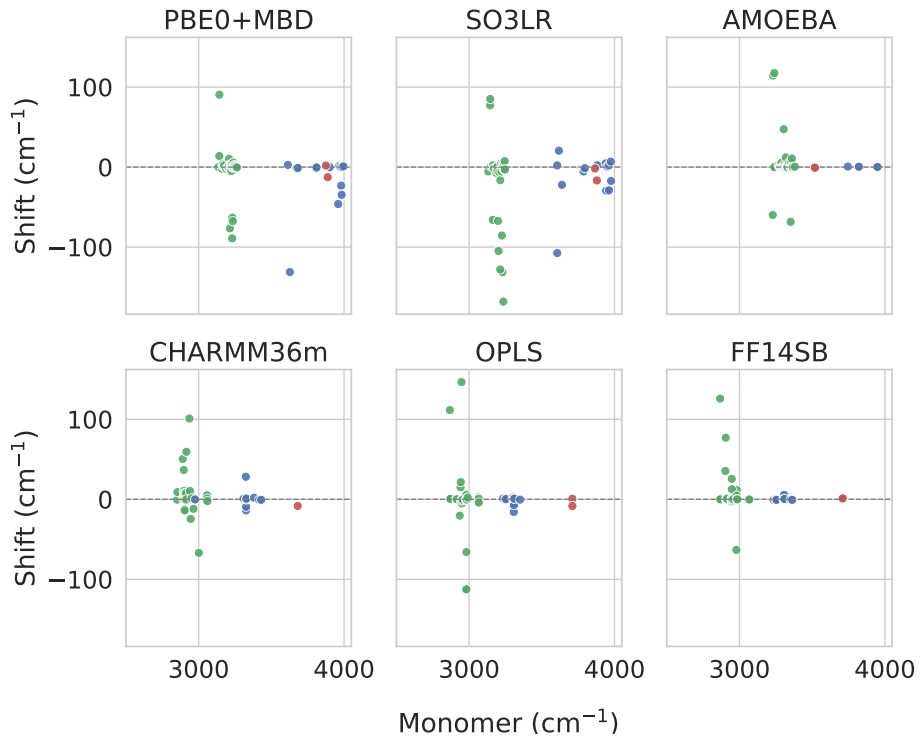


Fig. A12 High-frequency vibrational analysis of the β -sheet of p53 dimer (residues 227-333). Vibrational shifts (cm^{-1}) of high-frequency modes in dimer versus monomer. The x-axis is the monomer frequencies (cm^{-1}). Each point corresponds to the most similar mode matched by the atom index. Vibrational modes are color-coded as follows: green for C–H stretching, blue for N–H stretching and red for O–H stretching.

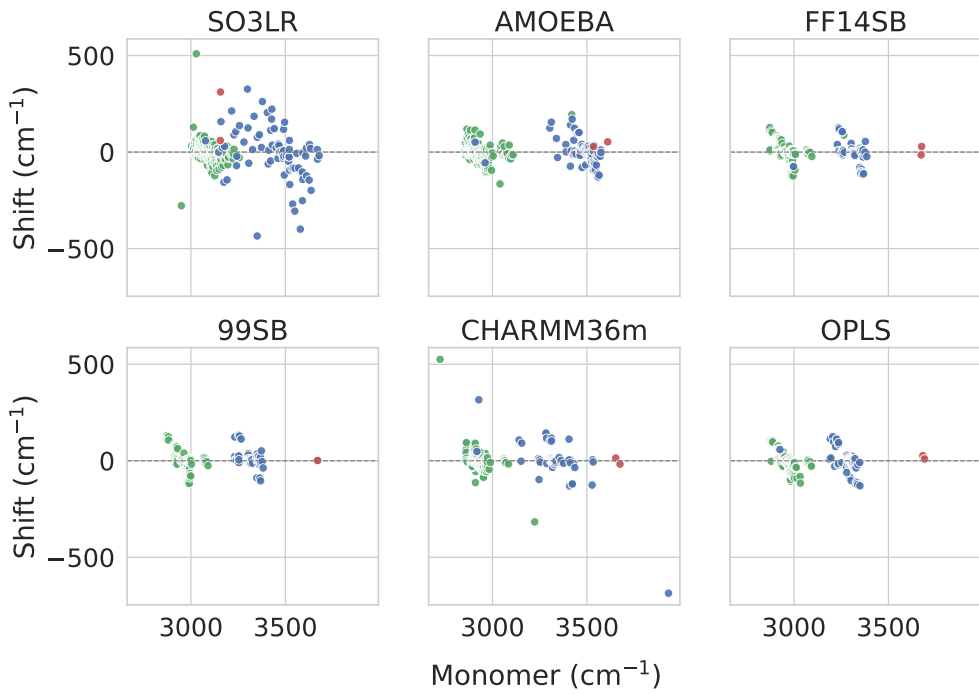


Fig. A13 High-frequency vibrational analysis of p53 tetramer and monomer in water. Vibrational shifts (cm^{-1}) of high-frequency modes in dimer versus monomer. The x-axis is the monomer frequencies (cm^{-1}). Each point corresponds to the most similar mode matched by the atom index. Vibrational modes are color-coded as follows: green for C–H stretching, blue for N–H stretching and red for O–H stretching.

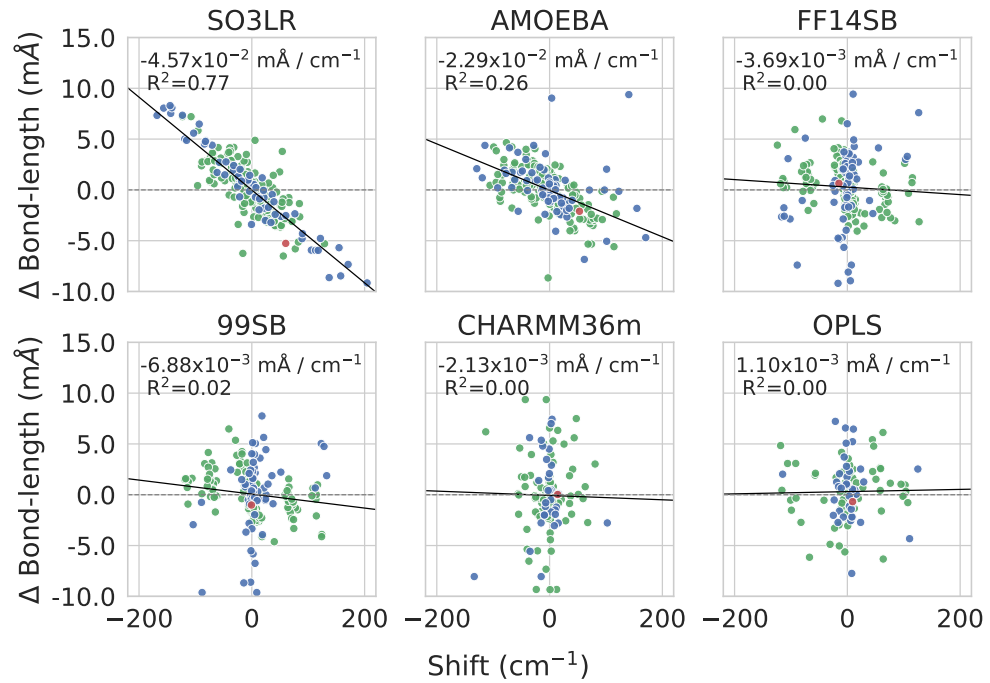


Fig. A14 Vibrational shifts plotted against bond-length differences between solvated tetramer and monomer configurations, including the linear correlation R^2 and the mÅ/cm $^{-1}$ slope. Vibrational modes are color-coded as follows: green for C–H stretching, blue for N–H stretching and red for O–H stretching.

Appendix B Amino Acids under Solvent Effects

Tyrosine, Leucine, and Arginine, each capped with Ace and NMe groups, were studied both in vacuum and in a water shell extending 3Å from the molecular atoms. The amino acids in vacuum were optimized using the PBE0+MBD functional with 'tight' settings, following the same approach described in the small molecule section. Subsequently, a larger shell of water molecules (8Å) was added to the optimized conformations. An energy minimization was performed using xtb [5] with the amino acid atoms fixed, allowing the surrounding water molecules to relax. After this step, a 3Å water shell was extracted. A second minimization cycle was then carried out, again constraining the amino acid atoms.

To ensure a fair comparison, the same conformers, both in vacuum and in water, were used across all methods. Normal mode analysis was performed as described in the Methods section.

B.1 Tyrosine

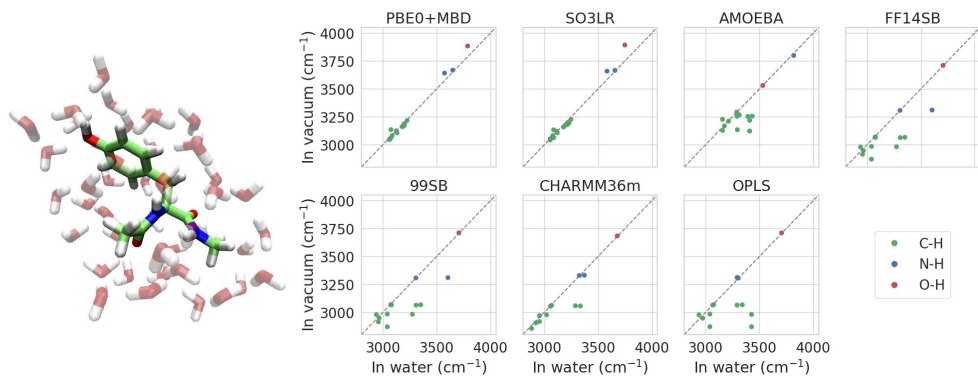


Fig. B15 Vibrational frequency shifts of high-frequency modes in water (x-axis) compared to vacuum (y-axis) for the Ace-Tyr-NMe amino acid, computed using PBE0+MBD, SO3LR, and the most commonly used empirical molecular force fields.

B.2 Leucine

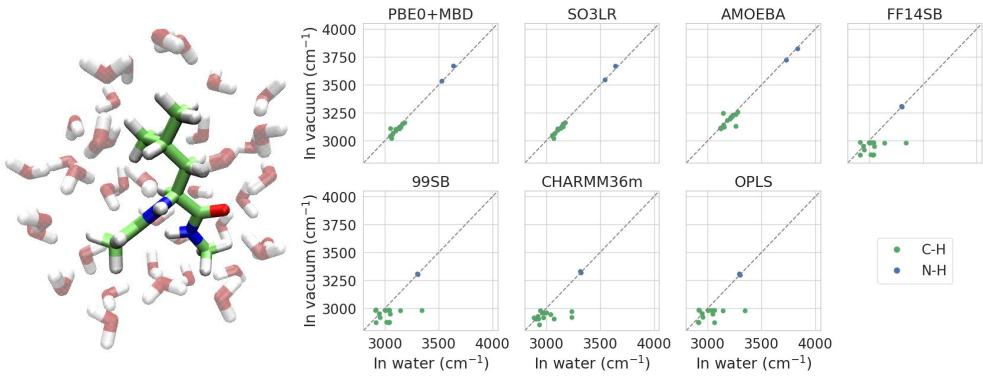


Fig. B16 Vibrational frequency shifts of high-frequency modes in water (x-axis) compared to vacuum (y-axis) for the Ace-Leu-NMe amino acid, computed using PBE0+MBD, SO3LR, and the most commonly used empirical molecular force fields.

B.3 Arginine

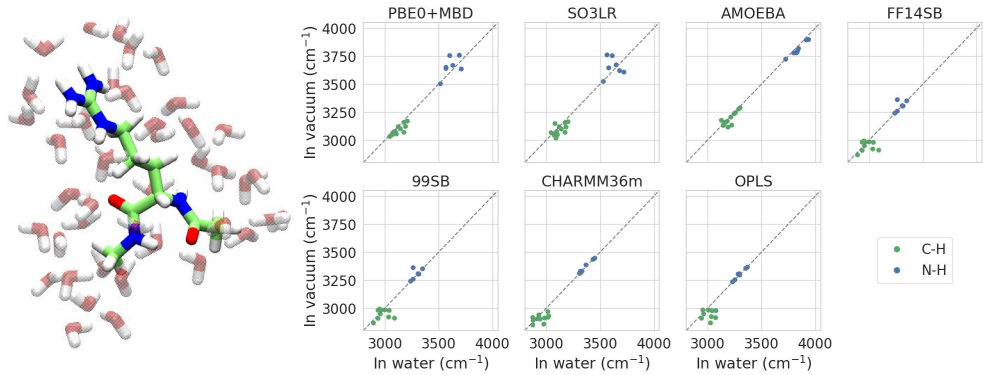


Fig. B17 Vibrational frequency shifts of high-frequency modes in water (x-axis) compared to vacuum (y-axis) for the Ace-Arg-NMe amino acid, computed using PBE0+MBD, SO3LR, and the most commonly used empirical molecular force fields.

References

- [1] Kochanov, R. *et al.* Infrared absorption cross-sections in HITRAN2016 and beyond: Expansion for climate, environment, and atmospheric applications. *J. Quant. Spectrosc. Radiat. Transf.* **230**, 172–221 (2019).

- [2] Gordon, I. E. *et al.* The HITRAN2020 molecular spectroscopic database. *J. Quant. Spectrosc. Radiat. Transf.* **277**, 107949 (2022).
- [3] of Standards, N. I. & Technology. Nist chemistry webbook, nist standard reference database number 69. [10.18434/T4D303](https://doi.org/10.18434/T4D303) (2025).
- [4] Frishman, D. & Argos, P. Knowledge-based protein secondary structure assignment. *Proteins: Structure, Function, and Bioinformatics* **23**, 566–579 (1995).
- [5] Bannwarth, C. *et al.* Extended tight-binding quantum chemistry methods. *WIREs Comput. Mol. Sci.* **11**, e1493 (2021).